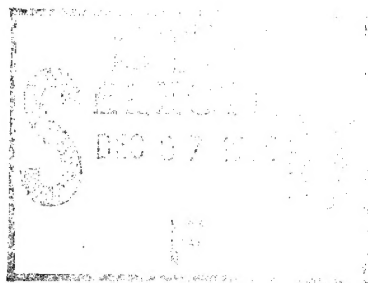


---

# **ELECTROMAGNETIC ANALYSIS OF PERIODIC STRUCTURE REFLECTION AND TRANSMISSION BY THE HYBRID FINITE ELEMENT METHOD**

**Daniel T. McGrath, Major, USAF**

**September 1995**



**Final Report**

---

**APPROVED FOR PUBLIC RELEASE; DISTRIBUTION IS UNLIMITED.**

---



**PHILLIPS LABORATORY  
Advanced Weapons and Survivability Directorate  
AIR FORCE MATERIEL COMMAND  
KIRTLAND AIR FORCE BASE, NM 87117-5776**

---

19951204 034

This final report was prepared by the Phillips Laboratory, Kirtland Air Force Base, New Mexico, under Job Order 3152AK06. The Laboratory Project Officer-in-Charge was Maj. Daniel T. McGrath (WSR).

When Government drawings, specifications, or other data are used for any purpose other than in connection with a definitely Government-related procurement, the United States Government incurs no responsibility or any obligation whatsoever. The fact that the Government may have formulated or in any way supplied the said drawings, specifications, or other data, is not to be regarded by implication, or otherwise in any manner construed, as licensing the holder, or any other person or corporation; or as conveying any rights or permission to manufacture, use, or sell any patented invention that may in any way be related thereto.

This report has been authored by an employee of the United States Government. Accordingly, the United States Government retains a nonexclusive royalty-free license to publish or reproduce the material contained herein, or allow others to do so, for the United States Government purposes.

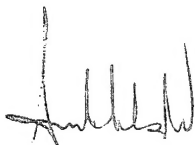
This report has been reviewed by the Public Affairs Office and is releasable to the National Technical Information Service (NTIS). At NTIS, it will be available to the general public, including foreign nationals.

If your address has changed, if you wish to be removed from the mailing list, or if your organization no longer employs the addressee, please notify PL/WSR, 3550 Aberdeen Ave SE, Kirtland AFB, NM 87117-5776, to help maintain a current mailing list.

This report has been reviewed and is approved for publication.

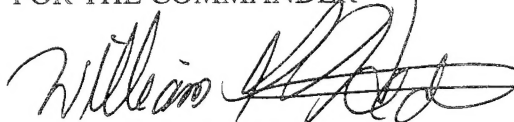


DANIEL T. McGRATH, Maj., USAF  
Deputy Chief, Electromagnetic Sources Division  
Project Officer



FORREST J. AGEE, GM-15  
Chief, Electromagnetic Sources  
Division

FOR THE COMMANDER



WILLIAM G. HECKATHORN, Colonel, USAF  
Director, Advanced Weapons  
and Survivability Directorate

DO NOT RETURN COPIES OF THIS REPORT UNLESS CONTRACTUAL OBLIGATIONS OR NOTICE ON A SPECIFIC DOCUMENT REQUIRES THAT IT BE RETURNED.

REPORT DOCUMENTATION PAGE			Form Approved OMB No. 0704-0188	
Public reporting burden for this collection of information is estimated to average 1 hour per response, including the time for reviewing instructions, searching existing data sources, gathering and maintaining the data needed, and completing and reviewing the collection of information. Send comments regarding this burden estimate or any other aspect of this collection of information, including suggestions for reducing this burden, to Washington Headquarters Services, Directorate for Information Operations and Reports, 1215 Jefferson Davis Highway, Suite 1204, Arlington, VA 22202-4302, and to the Office of Management and Budget, Paperwork Reduction Project (0704-0188), Washington, DC 20503.				
1. AGENCY USE ONLY (Leave blank)		2. REPORT DATE September 1995		3. REPORT TYPE AND DATES COVERED Final; Aug 93 - Sep 95
4. TITLE AND SUBTITLE ELECTROMAGNETIC ANALYSIS OF PERIODIC STRUCTURE REFLECTION AND TRANSMISSION BY THE HYBRID FINITE ELEMENT METHOD			5. FUNDING NUMBERS  PE: 63605F PR: 3152 TA: AK WU: 06	
6. AUTHOR(S)  Daniel T. McGrath, Major, USAF				
7. PERFORMING ORGANIZATION NAME(S) AND ADDRESS(ES)  Phillips Laboratory 3550 Aberdeen Avenue, SE Kirtland AFB, NM 87117-5776			8. PERFORMING ORGANIZATION REPORT NUMBER  PL-TR--95-1103	
9. SPONSORING / MONITORING AGENCY NAME(S) AND ADDRESS(ES)			10. SPONSORING / MONITORING AGENCY REPORT NUMBER	
11. SUPPLEMENTARY NOTES				
12a. DISTRIBUTION / AVAILABILITY STATEMENT  Approved for Public Release; Distribution Unlimited			12b. DISTRIBUTION CODE	
13. ABSTRACT (Maximum 200 words)  A numerical solution for the time-harmonic electromagnetic fields in an infinite periodic structure has been developed, implemented, and validated. It uses a variation of the hybrid finite element method that includes periodic radiation conditions at the exterior surfaces, and periodicity conditions at the unit cell side walls inside the structure. The electric fields inside the unit cell are represented by linear vector finite elements. The successful test cases include an inductive screen, a parallel wire grid, a conducting-sphere artificial dielectric, a bandgap structure made up of parallel, layered-dielectric rods, and crossed conducting bars representative of reinforced concrete. The report describes the formulation of the method, and its implementation in a general-purpose computer code, and the results of the test cases. Possible uses of the code for studies in high power microwaves are addressed.				
14. SUBJECT TERMS Electromagnetic Fields, Scattering, Filters Antenna Arrays, Windows, Filters, Polarizers Finite Element Analysis, Computer Programs			15. NUMBER OF PAGES 64	
			16. PRICE CODE	
17. SECURITY CLASSIFICATION OF REPORT Unclassified	18. SECURITY CLASSIFICATION OF THIS PAGE Unclassified	19. SECURITY CLASSIFICATION OF ABSTRACT Unclassified	20. LIMITATION OF ABSTRACT UL	

## TABLE OF CONTENTS

1. INTRODUCTION .....	1
2. BACKGROUND .....	2
2.1. Problem Description .....	2
2.2. Solution Method Overview .....	2
3. THEORY .....	6
3.1. The Weak Form of the Wave Equation .....	6
3.2. Finite Element Representation of the Electric Field .....	7
3.3. Interior Discretization .....	8
3.4. Mode Functions and the Periodic Integral Equation .....	11
3.5. Periodic Radiation Boundary Terms .....	14
3.6. Side Wall Periodicity Condition .....	15
3.6.1. Boundary Wrapping Concept .....	15
3.6.2. Matrix Transformation .....	16
3.6.3. Algorithmic Implementation .....	17
3.6.4. "Overlap Elements" on the Radiation Boundaries .....	18
3.7. Incident Field Terms .....	18
3.8. Transmissivity and Reflectivity .....	19
4. NUMERICAL IMPLEMENTATION .....	21
4.1. Geometry Generation .....	21
4.1.1. CAD Geometry Definition .....	21
4.1.2. Unit Cell Side Wall Geometry Definition .....	21
4.1.3. Conductor Boundary Conditions .....	23
4.1.4. Node-Based to Edge-Based Geometry Conversion .....	24
4.2. Matrix Data Structure and Computations .....	25
4.3. Matrix Solution .....	26
4.3.1. Conjugate Gradient Method .....	26
4.3.2. Biconjugate Gradient Method .....	27
5. VALIDATION .....	31
5.1. Inductive Screen Filter .....	31
5.2. Wire Grid Array .....	34

5.3. Artificial Dielectric . . . . .	36
5.4. Dielectric Bandgap Structure . . . . .	38
5.5. Reinforced Concrete . . . . .	41
5.6. Crossed Dipole Frequency Selective Surface . . . . .	43
5.7. Storage, Execution Time and Accuracy Issues . . . . .	45
6. CONCLUSIONS AND RECOMMENDATIONS . . . . .	48
REFERENCES . . . . .	50

## LIST OF FIGURES

1. Representative Problem Geometry: (a) Side view showing upper and lower radiation boundaries; (b) top view of array lattice showing unit cell boundaries . . . . .	3
2. Example Tetrahedron Mesh: Crossed Dipole FSS Element in Skewed Lattice . . . . .	4
3. Side View of Example Mesh - Surface Grid on Unit Cell Walls Only . . . . .	22
4. Direction and Sequence for Defining Curves and Mesh Areas to Achieve Identical Meshes on Opposing Unit Cell Side Walls: (a) Curve Directions; (b) Order of Selection for Curves to Make up Mesh Areas . . . . .	23
5. Convergence of Residual Norm, Reflectivity and Transmissivity using Conjugate Gradient Method . . . . .	28
6. Convergence of Residual Norm, Reflectivity and Transmissivity using Biconjugate Gradient Method . . . . .	30
7. Two-layer Inductive Screen . . . . .	32
8. Tetrahedron Mesh for a Unit Cell of the Two-layer Inductive Screen . . . . .	32
9. HFEM Calculations for Transmissivity of Two-layer Inductive Screen, Compared with Moment Method (Mode Matching) Results [19] . . . . .	33
10. Tetrahedron Mesh for Wire Grid Array . . . . .	35
11. Parallel-polarized Transmission through Wire Grid Array vs. Scan Angle . . . . .	35
12. Tetrahedron Mesh for a Conducting Sphere in a Cubic Lattice . . . . .	37
13. Differential Transmission Phase for a Single Layer of Artificial Dielectric . . . . .	38

14. Layered Dielectric Rod used to Simulate Photonic Band Structure . . . . .	39
15. Tetrahedron Mesh for Layered Dielectric Rods: (a) Exploded View of Single Rod; (b) Unit Cell Mesh for Four-layer Structure . . . . .	40
16. Comparison of Hybrid Finite Element Method Calculations and Measurements for 10-layer Dielectric Rod Array . . . . .	41
17. Cutaway of One Half of Tetrahedron Mesh for Reinforced Concrete Unit Cell . . . . .	43
18. Normal-incidence Transmission through 4"x4" Reinforcing Bar Lattice . . . . .	44
19. Oblique-incidence Transmission through 4"x4" Reinforcing Bar Lattice: $(\theta_0, \phi_0) = (30^\circ, 45^\circ)$ , Transverse Electric Polarization . . . . .	44
20. Crossed Dipole FSS Element and Lattice Geometry . . . . .	46
21. Comparison of HFEM and MoM Calculations of TM Reflection from Crossed Dipole Frequency Selective Surface $(\theta_0 = 30^\circ, \phi_0 = 0^\circ)$ . . . . .	46
22. Tetrahedron Mesh for Crossed Dipole Frequency Selective Surface Test Case: Two Air Layers Surround the Conducting Elements . . . . .	47
23. Number of Iterations vs. Frequency for Bandgap Structure . . . . .	49

## LIST OF TABLES

Table I. Mesh Sizes and Storage Requirements for Test Cases . . . . .	48
Table II. Iterations and Execution Times for Test Cases . . . . .	48

Accession For	
NTIS	<input checked="" type="checkbox"/>
DTIC	<input type="checkbox"/>
Unannounced	<input type="checkbox"/>
Justification	
Distribution /	
Availability Codes	
Dist	Avail and/or Special
A-1	



## 1. INTRODUCTION

Analysis and design of periodic structures is important to many areas of microwave and antenna engineering. For example, in designing equipment enclosures to suppress electromagnetic interference (EMI), one may need to know the amount of radio frequency (RF) penetration through periodic screens such as perforated metal, wire grids, or reinforced concrete. In antenna design, periodic structures may take the form of: frequency selective surfaces (FSSs) [1],[2], proposed for use as subreflectors and interference-suppressing radomes; polarizers [3]; artificial dielectrics [4] for lightweight lenses; and angular filters for sidelobe suppression [5]. Periodic structures also appear in the field of optics, as diffraction gratings and bandgap filters. But in optics, as in radio frequency applications, the behavior of these devices is essentially electromagnetic. In most cases, acceptable performance prediction is obtainable only with analytical methods that account for mutual interactions between elements of the structure. The available tools have, to date, been based on mode matching and moment methods. Their most significant limitations were: (1) inability to model "inhomogeneous" dielectrics (anything other than continuous planar slabs); and (2) restrictions on the shape and/or orientation of conducting elements, requiring a separate computer code for each of many classes of geometries. This report describes a new analysis technique that employs the hybrid finite element method (HFEM) in order to permit full wave analysis of very general periodic structures containing dielectric inhomogeneities and arbitrarily-oriented conductors. It is an extension of previous work in modeling phased array antennas [6].



## 2. BACKGROUND

### 2.1. Problem Description

The generic problem to be addressed is electromagnetic transmission through large, planar periodic structures. They are assumed to be large enough that edge effects are negligible, allowing use of an infinite structure model. This restricts the analysis to a single unit cell that is typically a fraction of a wavelength on each side at the frequencies at which the device is designed to operate. Figure 1 illustrates the general problem geometry and defines the notation conventions used throughout this report.

The structure may include conducting obstacles with arbitrary shape, and any number of dielectric regions with distinct permittivity,  $\epsilon$ , and permeability,  $\mu$ . The dielectrics are isotropic (their properties are not a function of direction) and linear (their properties do not depend on the magnitude of the fields). The structure lattice may be skewed, as illustrated in Figure 1b.

### 2.2. Solution Method Overview

The solution technique is a hybrid of the finite element method (FEM) with an integral equation representation for fields above and below the structure. The unit cell is truncated at planes of constant  $z$  above and below the structure so that all of the materials (dielectrics and conductors) are between the surfaces denoted  $\Gamma_{z-}$  and  $\Gamma_{z+}$ , which will be referred to as the lower and upper radiation boundaries, respectively. The volume thus formed by the truncated unit cell will be denoted by  $\Omega$ .

The free space and dielectrics inside  $\Omega$  will be subdivided into small volume elements (tetrahedra), referred to as "cells." The electric field will be represented in terms of simple expansion functions or "finite elements" defined relative to cells. The particular form used in

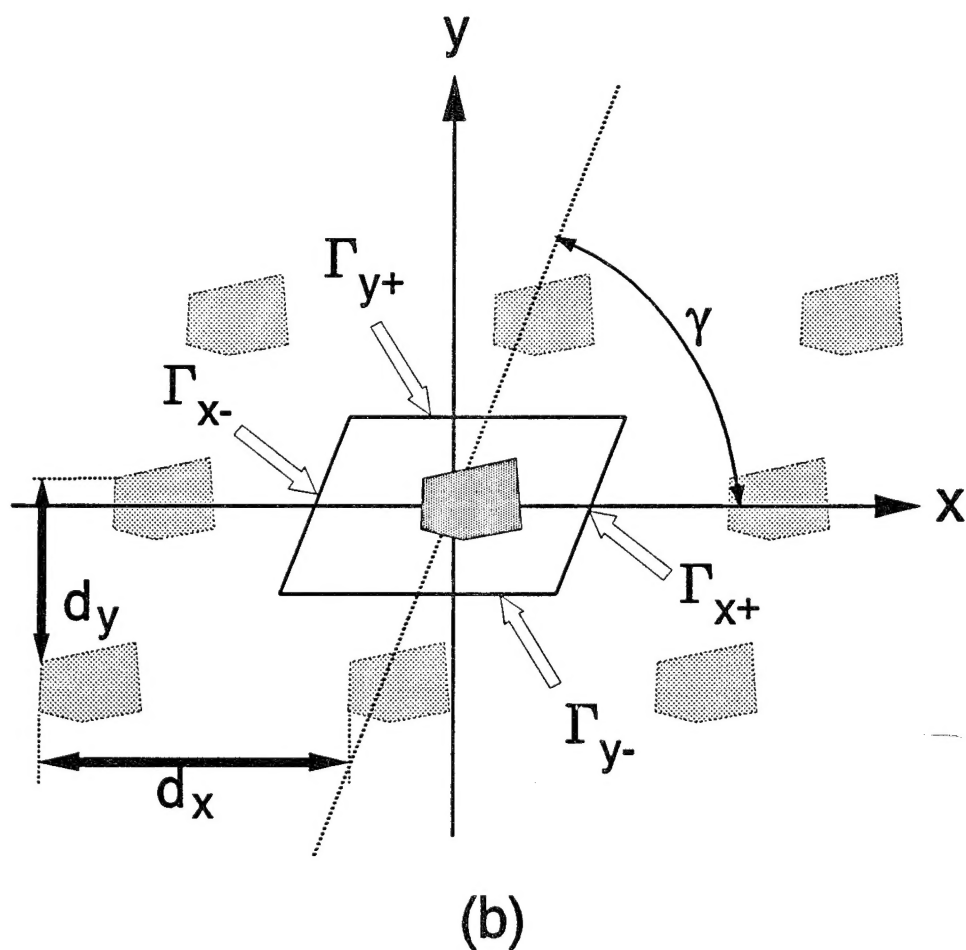
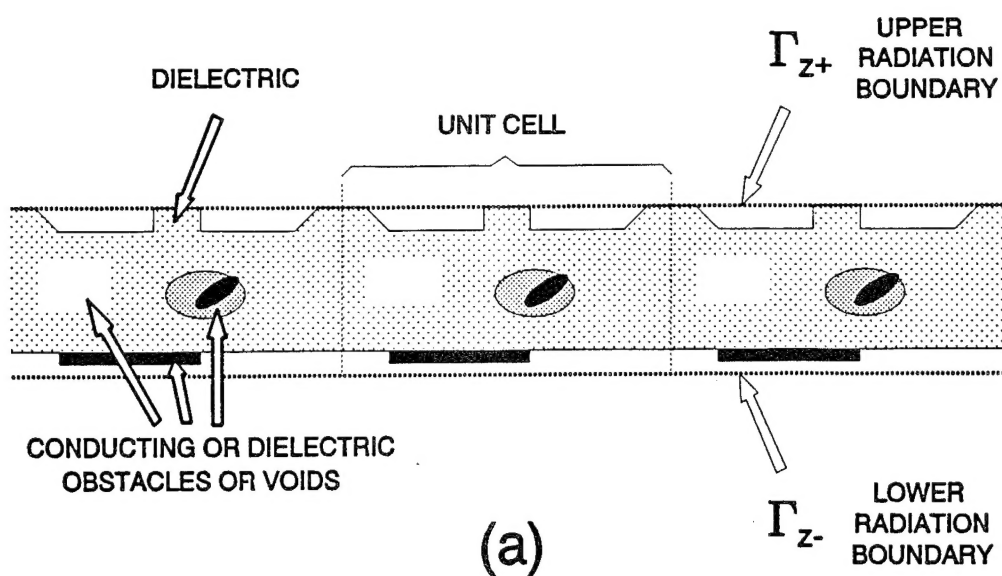


Figure 1. Representative Problem Geometry: (a) Side view showing upper and lower radiation boundaries; (b) top view of array lattice showing unit cell boundaries

this work is the linear vector edge-based finite elements. Figure 2 shows an example tetrahedron "mesh" for an FSS made up of a skewed lattice of crossed dipoles backed by a dielectric layer. The shading shows the location of the conducting elements, which are represented here by infinitesimally thin conductors. Thick conductors would be represented as voids in the mesh.

There are two kinds of periodic boundary conditions to be enforced. One is the periodic radiation condition, which expands the fields above and below the structure in terms of "Floquet modes." The second condition enforces periodicity across unit cell side walls.

The solution is implemented by constructing and solving a matrix equation:

$$[R][S^{\Gamma^-} + S^I + S^{\Gamma^+}][R]^H E = E^{inc} \quad (1)$$

The matrix  $S^I$  is a sparse matrix arising from the interior finite element solution. Its size is  $N \times N$ , where  $N$  is the number of edges in the tetrahedron grid, excluding those lying along

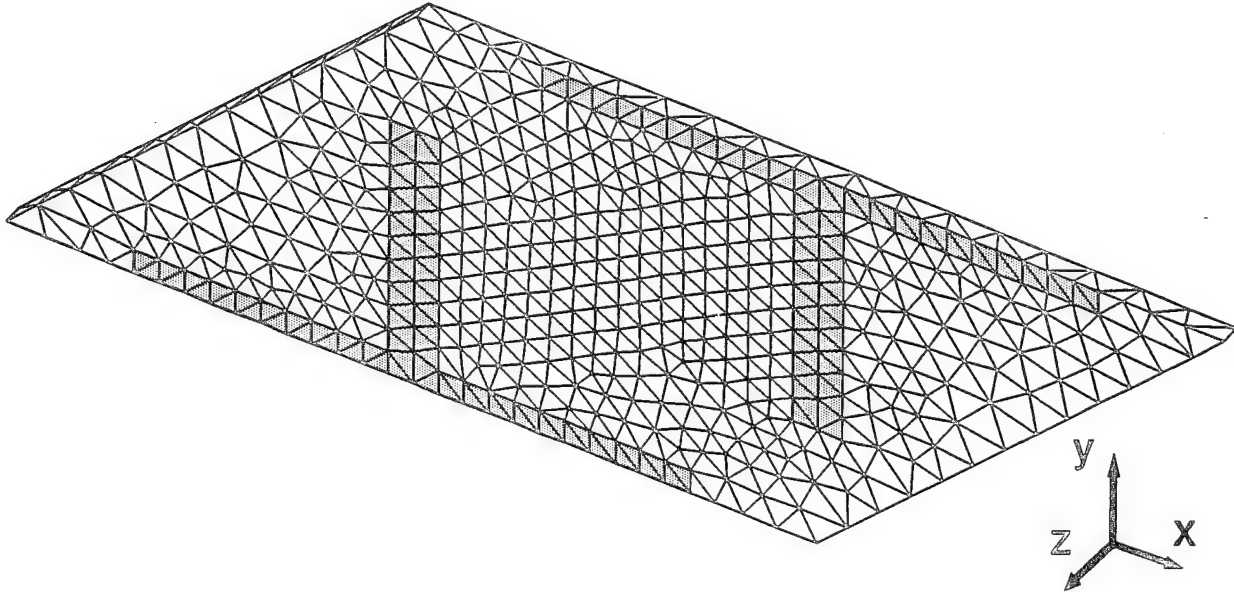


Figure 2. Example Tetrahedron Mesh: Crossed Dipole FSS Element in Skewed Lattice

perfectly conducting surfaces. Assuming that the edges are ordered so that the first are in  $\Gamma_{z-}$  and the last are in  $\Gamma_{z+}$ , then the matrices  $S^{\Gamma-}$  and  $S^{\Gamma+}$  due to the periodic radiation conditions, are zero except for dense upper left and lower right submatrices, respectively. Finally, multiplication on the left by the matrix  $R$  and on the right by its Hermitian (conjugate transpose) implements the side wall periodicity condition. The right side vector  $\mathbf{E}^{\text{inc}}$  is due to a unit-amplitude plane wave (the dominant Floquet mode). Its entries are zero except for those corresponding to edges in  $\Gamma_{z-}$ . Solution of the system of equations gives the vector  $\mathbf{E}$ , from which reflectivity and transmissivity are computed.

The following chapter will give the details of how each of the terms in the above matrix equation is derived from electromagnetic theory and from the methods of finite elements. Chapter 4 will discuss how it was implemented in a general-purpose computer code. Chapter 5 will show the results for several validation and demonstration cases.

### 3. THEORY

#### 3.1. The Weak Form of the Wave Equation

Finite element solutions are usually based on discretization of a "variational principle" or of a "weak form." Application of the Rayleigh-Ritz method to the variational principle results in the same matrix equation as does application of Galerkin's method to the weak form [6:102-103].

The wave equation for the electric field in linear, isotropic, inhomogeneous media is

$$\nabla \times \frac{1}{\mu_r} \nabla \times \bar{E} - k_0^2 \epsilon_r \bar{E} = 0 \quad (2)$$

where  $k_0$  is the free space wavenumber, and the relative permeability,  $\mu_r$ , and permittivity,  $\epsilon_r$ , may be functions of position. The inner product of (2) with a weighting function  $\bar{W}$  is

$$\int_{\Omega} \bar{W}^* \cdot \left[ \nabla \times \frac{1}{\mu_r} \nabla \times \bar{E} - k_0^2 \epsilon_r \bar{E} \right] dv = 0 \quad (3)$$

Using a Green's identity:

$$\int_{\Omega} \left[ \frac{1}{\mu_r} \nabla \times \bar{W}^* \cdot \nabla \times \bar{E} - k_0^2 \epsilon_r \bar{W}^* \cdot \bar{E} \right] dv - \int_{\Gamma} \frac{1}{\mu_r} \bar{W}^* \times \nabla \times \bar{E} \cdot \hat{n} ds = 0 \quad (4)$$

where  $\Gamma$  is the union of all boundaries enclosing  $\Omega$  as well as conducting surfaces inside  $\Omega$ . Equation (4) is called a "weak form" because the Green's identity shifted one of the derivatives from  $\bar{E}$  to  $\bar{W}$ , weakening the differentiability requirement on  $\bar{E}$ . The final form is obtained by using the Maxwell curl equation  $\nabla \times \bar{E} = -j\omega\mu\bar{H}$  and the constitutive relation  $\omega\mu = k_0\eta$ :

$$\int_{\Omega} \left[ \frac{1}{\mu_r} \nabla \times \bar{W}^* \cdot \nabla \times \bar{E} - k_0^2 \epsilon_r \bar{W}^* \cdot \bar{E} \right] dv - j k_0 \eta_0 \int_{\Gamma} \bar{W}^* \cdot (\hat{n} \times \bar{H}) ds = 0 \quad (5)$$

The term on the right, a surface integral over all boundaries enclosing  $\Omega$ , provides the mechanism for enforcing boundary conditions. On the open parts of  $\Gamma$ , suitable expressions for the tangential magnetic field may be substituted to impose radiation boundary conditions, as discussed in Section 3.4.

For perfect conductors, the second integral above becomes zero. The tangential electric field is zero, so admissible functions for  $\bar{E}$ , and hence also for  $\bar{W}$ , are those whose tangential component vanishes at a perfectly conducting boundary.

### 3.2. Finite Element Representation of the Electric Field

The electric field will be expanded in "finite elements," which are functions defined locally within each tetrahedral cell. The "linear edge elements" are defined relative to two mesh nodes  $i$  and  $j$  that bound a mesh edge [7]-[9]:

$$\bar{\psi}_{ij} = L_{ij}(f_i \nabla f_j - f_j \nabla f_i) \quad (6)$$

where  $L_{ij}$  is the length of the edge. The scalar functions  $f_i$  and  $f_j$  have the value 1 at node  $i$  or  $j$ , respectively, and decrease linearly to 0 at the other three nodes in the cell. The vector function  $\bar{\psi}_{ij}$  is normal to the faces opposite nodes  $i$  and  $j$ . Its component along edge  $ij$  is a unit vector. Now the electric field is approximated by

$$\bar{E} \approx \tilde{E} = \sum_{s=1}^N e_s \bar{\psi}_s(x, y, z) \quad (7)$$

where  $e_s$  is a scalar, complex coefficient representing the field magnitude and phase along the

edge  $s$ . This expansion makes it a trivial matter to enforce boundary conditions along perfect conductors, even at sharp edges and points. It also ensures that spurious modes will not be generated [10]. Furthermore, it correctly enforces continuity of the normal electric field across dielectric interfaces [11]. All three of these are reasons it is preferred over the scalar expansion  $\bar{E} \approx \sum \bar{e}_t f_t$  (defined relative to nodes).

### 3.3. Interior Discretization

The elements of the sparse matrix  $S^I$  in (1) are due to the volume integral term in (5). Substituting the expansion (7) for  $\bar{E}$  and using each  $\bar{\psi}_t$  in turn as a weighting function (Galerkin's method):

$$S_{st}^I = \int_{\Omega_{st}} \left[ \mu_r^{-1} \nabla \times \bar{\psi}_t \cdot \nabla \times \bar{\psi}_s - k_0^2 \epsilon_r \bar{\psi}_t \cdot \bar{\psi}_s \right] dv \quad (8)$$

where  $\Omega_{st}$  denotes the union of all cells that share edges  $s$  and  $t$ .

The integrations in (8) are carried out with the help of a coordinate transform local to each tetrahedron (called "simplex" or "barycentric" coordinates) [12:266-274]. Let  $U$  denote the matrix formed using the four vertex coordinates:

$$U = \begin{bmatrix} 1 & x_1 & y_1 & z_1 \\ 1 & x_2 & y_2 & z_2 \\ 1 & x_3 & y_3 & z_3 \\ 1 & x_4 & y_4 & z_4 \end{bmatrix} \quad (9)$$

and let  $T$  be the matrix of the 16 cofactors of  $U$ . There are four coordinate directions  $t_1 \dots t_4$  in the tetrahedron given by

$$t_i = \frac{1}{6V} [T_{i1} + xT_{i2} + yT_{i3} + zT_{i4}] \quad (10)$$

where  $V$  is the cell volume. Since  $t_i$  is equal to unity at node  $i$  and goes linearly to zero at all other nodes, it is the correct form for the scalar finite element function, and  $f_i = t_i$ . The gradient of  $f_i$  is

$$\nabla f_i = \frac{1}{6V} [\hat{x}T_{i2} + \hat{y}T_{i3} + \hat{z}T_{i4}] \quad (11)$$

The curl of the finite element,  $\nabla \times \bar{\psi}_s$ , is also needed in evaluating the integrals in (8). For that, the following vector identity is used:

$$\nabla \times (f_i \nabla f_j) = f_i \nabla \times \nabla f_j + \nabla f_i \times \nabla f_j \quad (12)$$

Note that the first term on the right in (12) is zero since it is a second derivative of a linear function. Consequently,

$$\begin{aligned} \nabla \times \bar{\psi}_s &= \nabla \times (f_i \nabla f_j - f_j \nabla f_i) \\ &= 2 \nabla f_i \times \nabla f_j \end{aligned} \quad (13)$$

To evaluate the contribution of a cell  $k$  to (8), let  $i$  and  $j$  denote the local indices of the nodes bounding edge  $s$ ; and let  $m$  and  $n$  denote those for edge  $t$ . All four of these local node indices are between 1 and 4. The first integral term in (8) will be

$$S_{stk}^{I1} = \frac{4V_k}{\mu_r} L_s L_t \nabla f_i \times \nabla f_j \cdot \nabla f_m \times \nabla f_n \quad (14)$$

$$\begin{aligned} &= \frac{4V_k L_s L_t}{\mu_r (6V_k)^2} [ (T_{i3}T_{j4} - T_{i4}T_{j3})(T_{m3}T_{n4} - T_{m4}T_{n3}) \\ &\quad + (T_{i4}T_{j2} - T_{i2}T_{j4})(T_{m4}T_{n2} - T_{m2}T_{n4}) \\ &\quad + (T_{i2}T_{j3} - T_{i3}T_{j2})(T_{m2}T_{n3} - T_{m3}T_{n2}) ] \end{aligned} \quad (15)$$



And the second volume integral term in (8) will be

$$S_{stk}^{I2} = -k_0^2 \epsilon_r L_s L_t \int_{\Omega_k} [f_i f_m \nabla f_j \cdot \nabla f_n - f_j f_m \nabla f_i \cdot \nabla f_n - f_i f_n \nabla f_j \cdot \nabla f_m + f_j f_n \nabla f_i \cdot \nabla f_m] dv \quad (16)$$

Since the gradient terms in (15) are constants, they may be taken outside the integral, leaving four terms of the form

$$I_{ij} = \int_{\Omega_k} f_i f_j dx dy dz \quad (17)$$

which transform to simplex coordinates as [12]

$$I_{ij} = 6 V_k \int_0^1 dt_i \int_0^{1-t_i} dt_j \int_0^{1-t_i-t_j} t_i t_j dt_m \quad (18)$$

where  $1/6V_k$  is the Jacobian of the transformation. This integral evaluates to

$$I_{ij} = \frac{V_k}{20} (1 + \delta_{ij}) \quad (19)$$

where  $\delta_{ij}$  is the Kronecker delta. Finally, (16) reduces to

$$S_{stk}^{I2} = -\frac{k_0^2 \epsilon_r L_s L_t}{720 V_k} \sum_{l=2}^4 [(1 + \delta_{im}) T_{jl} T_{nl} - (1 + \delta_{jm}) T_{il} T_{nl} - (1 + \delta_{in}) T_{jl} T_{ml} + (1 + \delta_{jn}) T_{il} T_{ml}] \quad (20)$$

Each matrix entry  $S_{st}^I$  is the sum of contributions from (15) and (20) from all cells that share edges  $s$  and  $t$ . Thus, those two equations give the interior matrix entries as closed-form algebraic expressions that depend only on the cell geometry, its constitutive parameters, and the wave-number. The following two sections show the derivation for the entries in the matrices pertain-

ing to the radiation boundaries.

### 3.4. Mode Functions and the Periodic Integral Equation

The top and bottom of the unit cell are free space boundaries where a radiation condition must be applied. The method for doing so is to substitute an integral equation for  $\hat{n} \times \bar{H}$  into the boundary term of the weak form. Due to the periodic nature of the problem, the integral equation may be written as a summation over "Floquet modes" [13].

Let the electric field above and below the structure be expanded in a set of mode functions  $\bar{g}_{pmn}$ , where the subscript  $p$  is 1 for transverse electric (i.e.  $\bar{E} \perp z$ ) or 2 for transverse magnetic (i.e.  $\bar{H} \perp z$ ):

$$\bar{g}_{pmn} = \bar{h}_{pmn} e^{j(k_{xmn}x + k_{ymn}y)} \quad (21)$$

$$\bar{h}_{1mn} = \frac{(\hat{x} k_{ymn} - \hat{y} k_{xmn})}{\sqrt{d_x d_y} \sqrt{k_{xmn}^2 + k_{ymn}^2}} \quad (22)$$

$$\bar{h}_{2mn} = \frac{(\hat{x} k_{xmn} + \hat{y} k_{ymn})}{\sqrt{d_x d_y} \sqrt{k_{xmn}^2 + k_{ymn}^2}} \quad (23)$$

$$k_{xmn} = k_0 \sin \theta_0 \cos \phi_0 - \frac{2\pi m}{d_x} \quad (24)$$

$$k_{ymn} = k_0 \sin \theta_0 \sin \phi_0 - \frac{2\pi n}{d_y} + \frac{2\pi m \cot \gamma}{d_x} \quad (25)$$

where  $(\theta_0, \phi_0)$  is the angle toward which the incident wave is propagating,  $(m, n)$  is the mode index and  $\gamma$  is the lattice skew angle.

At any point above the structure, the transverse electric field may be expanded in modes traveling in the +z direction:

$$\bar{E}^t(z > 0) = \sum_{p=1}^2 \sum_{m=-\infty}^{\infty} \sum_{n=-\infty}^{\infty} C_{pmn}^+ \bar{g}_{pmn} e^{-j\kappa_{mn}z} \quad (26)$$

$$\kappa_{mn} = [k_0^2 - k_{xmn}^2 - k_{ymn}^2]^{1/2} \quad (27)$$

where  $C_{pmn}^+$  is an unknown coefficient. The transverse magnetic field in each mode is

$$\hat{z} \times \bar{H}_{pmn}^t(z > 0) = -Y_{pmn} \bar{E}_{pmn}^t \quad (28)$$

where  $Y_{pmn}$  is a modal admittance:

$$Y_{1mn} = \frac{\kappa_{mn}}{k_0 \eta_0} \quad (29)$$

$$Y_{2mn} = \frac{k_0}{\kappa_{mn} \eta_0} \quad (30)$$

The total magnetic field above the structure is

$$\hat{z} \times \bar{H}^t(z > 0) = - \sum_p \sum_m \sum_n C_{pmn}^+ Y_{pmn} \bar{g}_{pmn} e^{-j\kappa_{mn}z} \quad (31)$$

In order to write the right side in terms of  $\bar{E}^t$ , the orthogonality property

$$\int_{\text{unit cell}} \bar{g}_{pmn} \cdot \bar{g}_{qij}^* dx dy = \delta_{pq} \delta_{mi} \delta_{nj} \quad (32)$$

is used to solve (26) for the coefficients:

$$C_{pmn}^+ = \int_{\text{unit cell}} \bar{E}^t \cdot \bar{g}_{pmn}^* dx dy \quad (33)$$

with the result

$$\hat{z} \times \bar{H}^t(z > 0) = - \sum_p \sum_m \sum_n Y_{pmn} \bar{g}_{pmn} \int_{\text{unit cell}} \bar{E}^t \cdot \bar{g}_{pmn}^* dx dy e^{-j\kappa_{mn}z} \quad (34)$$

On the lower unit cell boundary, the transverse electric field includes an incident field term in one of the two lowest order modes depending on whether it is transverse electric ( $q=1$ ) or transverse magnetic ( $q=2$ ):

$$\bar{E}^t(z < 0) = \bar{g}_{q00} e^{-j\kappa_{00}z} + \sum_{p=1}^2 \sum_{m=-\infty}^{\infty} \sum_{n=-\infty}^{\infty} C_{pmn}^- \bar{g}_{pmn} e^{j\kappa_{mn}z} \quad (35)$$

The signs of the exponential terms indicate the direction of propagation. Again, using the modes' orthogonality property,

$$C_{pmn}^- = \int_{\text{unit cell}} \bar{E}^t \cdot \bar{g}_{pmn}^* dx dy - \delta_{pq} \delta_{m0} \delta_{n0} \quad (36)$$

giving the magnetic field below the structure as

$$\begin{aligned} \hat{z} \times \bar{H}^t(z < 0) = & - \sum_p \sum_m \sum_n Y_{pmn} \bar{g}_{pmn} \int_{\text{unit cell}} \bar{E}^t \cdot \bar{g}_{pmn}^* dx dy e^{j\kappa_{mn}z} \\ & + 2 Y_{q00} \bar{g}_{q00} e^{-j\kappa_{mn}z} \end{aligned} \quad (37)$$

The above expressions (34) and (37) are the integral equations that are substituted into the weak form (5) to enforce the radiation conditions. The following section derives expressions for the resulting matrix terms.

### 3.5. Periodic Radiation Boundary Terms

The matrix entries  $S_{st}^{\Gamma+}$ , pertaining to the upper radiation boundary, are found by substituting  $\bar{\psi}_s$  for  $\bar{E}^t$  in (34), then substituting (34) for  $\hat{n} \times \bar{H}$  and  $\bar{\psi}_t$  for  $\bar{W}^*$  in Eq. (5):

$$S_{st}^{\Gamma+} = +jk_0\eta_0 \int_{\Gamma_{z+}} \bar{\psi}_t \cdot \sum_p \sum_m \sum_n Y_{pmn} \bar{g}_{pmn} dx dy \int_{\Gamma_{z+}} [\bar{\psi}_s \cdot \bar{g}_{pmn}^*] dx dy e^{-jk_{mn}z} \quad (38)$$

Each integral term contains a term in  $\exp\{\pm j(k_{xmn}x + k_{ymn}y)\}$ , which, besides the finite elements, is the only term with x or y dependence. Let  $\bar{\xi}_t(k_x, k_y)$  denote the two-dimensional Fourier transform of that part of  $\bar{\psi}_t$  lying on the radiation boundary:

$$\begin{aligned} \int_{\Gamma_{z+}} \bar{\psi}_t \cdot \bar{g}_{pmn} dx dy &= \bar{h}_{pmn} \cdot \int_{\Gamma_{z+}} \bar{\psi}_t e^{j(k_{xmn}x + k_{ymn}y)} dx dy \\ &= \bar{h}_{pmn} \cdot \bar{\xi}_t(k_{xmn}, k_{ymn}) \\ &= \bar{h}_{pmn} \cdot \bar{\xi}_{tmn} \end{aligned} \quad (39)$$

Now the matrix entries may be written in the more compact form

$$S_{st}^{\Gamma+} = jk_0\eta_0 \sum_p \sum_m \sum_n \bar{\xi}_{tmn} \cdot [Y_{pmn} \bar{h}_{pmn} \bar{h}_{pmn}] \cdot \bar{\xi}_{smn}^* \quad (40)$$

Finally, the term in brackets may be simplified by summing TE and TM modes:

$$S_{st}^{\Gamma+} = jk_0\eta_0 \sum_m \sum_n \bar{\xi}_{tmn} \cdot \tilde{T}_{mn} \cdot \bar{\xi}_{smn}^* \quad (41)$$

$$\tilde{T}_{mn} = \frac{[k_0^2 - k_{xmn}^2 - k_{ymn}^2]^{-1/2}}{d_x d_y k_0 \eta_0} \begin{bmatrix} (k_0^2 - k_{ymn}^2) & k_{xmn} k_{ymn} \\ k_{xmn} k_{ymn} & (k_0^2 - k_{xmn}^2) \end{bmatrix} \quad (42)$$

The expression for the matrix pertaining to the lower radiation boundary is identical to (41).

This follows from the fact that the summations in (35) and (37) are the same except for the sign of the exponent inside the integral. In evaluating those integrals, the value of  $z$  in the exponent is taken as zero because it represents only a constant phase factor.

This concludes the derivations for the entries in various parts of the matrix  $S$ . The following section discusses the matrix transformation that imposes a periodicity condition on the open unit cell side walls.

### 3.6. Side Wall Periodicity Condition

#### 3.6.1. Boundary Wrapping Concept

To understand how the transformation matrix  $R$  in (1) is created, it is important to recognize that the unit cell mesh is actually part of an "infinite mesh." A portion of the mesh is replicated identically within each unit cell. An essential requirement is that the mesh continues unbroken across unit cell boundaries, which implies that the mesh on a unit cell side wall is an exact replica of that on the opposing side wall. Section 4.1.2 will discuss how to accomplish this "mesh continuity" using a typical commercial mesh generation program.

The system of equations formed by (15), (20) and (41) contains one unknown per mesh edge. But because of the Floquet condition, the fields on opposite side walls are identical except for a constant and known phase shift that depends only on the unit cell size and the scan angle. Consequently, the linear system is *overdetermined* because there is a linear dependence between unknowns associated with image edges. For example, if  $e_s$  is the electric field along an edge in  $\Gamma_{x+}$ , then the field along the corresponding edge in  $\Gamma_{x-}$  is

$$e_{s'} = e_s e^{j\beta_x d_x}, s \in \Gamma_{x+}, s' \in \Gamma_{x-} \quad (43)$$

$$\beta_x = k_0 \sin\theta_0 \cos\phi_0 \quad (44)$$

Similarly, the fields for corresponding edges in  $\Gamma_{y+}$  and  $\Gamma_{y-}$  are related by

$$e_{s'} = e_s e^{j(\beta_x d_y \cot\gamma + \beta_y d_y)}, s \in \Gamma_{y+}, s' \in \Gamma_{y-} \quad (45)$$

$$\beta_y = k_0 \sin\theta_0 \sin\phi_0 \quad (46)$$

Because of this dependence, the linear system may not be solved until it is reduced by combining dependent rows and columns.

One way of viewing the reduction procedure is the following: The infinite mesh will be recreated from the unit cell mesh by "wrapping" opposite sides onto each other with an appropriate phase shift. This will merge the image edges, thus eliminating dependent unknowns from the linear system. There are two implementations: the matrix transformation indicated in Eq. (1), and algorithmic implementation.

### 3.6.2. Matrix Transformation

The matrix transformation is executed by multiplying on the left by a reduction matrix  $R$  and on the right by its Hermitian. This relies on a special ordering of the unknowns, with those in the side walls last, so that they make up the lower right portion of the matrix  $S$ .

$R$  is  $M \times N$ , where  $N-M$  is the number of edges on  $\Gamma_{x+}$  and  $\Gamma_{y+}$  combined. Its first  $M$  columns are the  $M \times M$  identity matrix. In the remaining columns, there is an entry  $R_{ik}$  for each pair of image edges:

$$R_{ik} = \begin{cases} e^{j\beta_x d_x}, & k \in \Gamma_{x+}, i \in \Gamma_{x-} \\ e^{j(\beta_x d_y \cot \gamma + \beta_y d_y)}, & k \in \Gamma_{y+}, i \in \Gamma_{y-} \\ e^{j(\beta_x d_x + \beta_y d_y \cot \gamma + \beta_y d_y)}, & k \in \Gamma_{x+} \cap \Gamma_{y+}, i \in \Gamma_{x-} \cap \Gamma_{y-} \end{cases} \quad (47)$$

### 3.6.3. Algorithmic Implementation

It is not actually necessary to impose the side wall condition as a matrix multiplication, and it is actually undesirable since it requires additional computer storage. The same end result is obtained by executing the following algorithm. It has the added advantage that the edges do not have to be ordered with those in the side walls last.

I. FOR EVERY EDGE  $s$  ON  $+x$  BOUNDARY:

A. LOCATE IMAGE EDGE  $s'$  ON  $-x$  BOUNDARY

B. FOR EVERY EDGE  $t$  SUCH THAT  $S_{st} \neq 0$ :

1. IF  $t$  IS ON THE  $+x$  BOUNDARY, THEN:

a. LOCATE IMAGE EDGE  $t'$

b. SET  $S_{s't'} = S_{s't'} + S_{st}$

c. SET  $S_{st} = 0$

2. ELSE IF  $t$  IS NOT ON THE  $+x$  BOUNDARY, THEN:

a. SET  $S_{s't} = S_{st} \exp\{j\beta_x\}$

b. SET  $S_{ts'} = S_{ts} \exp\{-j\beta_x\}$

c. SET  $S_{st} = S_{ts} = 0$

II. REPEAT I FOR  $+y$  AND  $-y$  BOUNDARIES

III. COMPRESS THE MATRIX (ELIMINATE ZERO ROWS & COLUMNS)

IV. COMPRESS THE INCIDENT FIELD VECTOR



### 3.6.4. "Overlap Elements" on the Radiation Boundaries

The two periodicity conditions, one for side walls and the other for radiation boundaries, must work in concert, neither duplicating nor opposing each other. Gedney first establish a straightforward method for doing so in two dimensions, which he called "overlap elements" [14]. In computing the terms of (1) pertaining to the radiation boundaries, those edges in  $\Gamma_{x+}$  and  $\Gamma_{y+}$  are ignored. There are no terms in  $S^{\Gamma+}$  or  $S^{\Gamma-}$  for those edges. However, edges in  $\Gamma_{x-}$  and  $\Gamma_{y-}$  are treated as though they were part of triangular elements extending into adjacent unit cells. That is, the finite elements connected to those edges "overlap" the unit cell boundaries. This method actually results in a simpler algorithm than Eq. (1) suggests, since the matrix transform need only be applied to  $S^I$ .

### 3.7. Incident Field Terms

The right side vector in the matrix equation arises from the second term on the right side of (37), due to a unit amplitude incident electric field arriving from  $z < 0$ . Its form is a plane wave, which is the 0,0-order Floquet mode. Along edge  $t$ :

$$e_t^{inc} = -jk_0 \eta_0 \int_{\Gamma_{z-}} \bar{\psi}_t \circ (2 Y_{q00} \bar{g}_{q00}) dx dy \quad (48)$$

where, again, the constant phase factor  $\exp\{-j \kappa_{mn} z\}$  is ignored. Taking all of the terms outside the integral that do not depend on  $x$  and  $y$ :

$$e_t^{inc} = -2jk_0 \eta_0 Y_{q00} \bar{h}_{q00} \circ \int_{\Gamma_{z-}} \bar{\psi}_t e^{j(k_{x00}x + k_{y00}y)} dx dy \quad (49)$$

Note that the integral is the two-dimensional Fourier transform of the finite element's tangential

component on  $\Gamma_z$ , written as  $\bar{\xi}_{t00}$ . Note also that:

$$k_{x00}^2 + k_{y00}^2 = k_0^2 \sin^2 \theta_0 \quad (50)$$

$$Y_{q00} = \begin{cases} \frac{\cos \theta_0}{\eta_0} & q = 1 \\ \frac{1}{\eta_0 \cos \theta_0} & q = 2 \end{cases} \quad (51)$$

and now (49) may be rewritten in the form

$$E_t^{inc} = \frac{-2j k_0}{\sqrt{d_x d_y}} \begin{cases} \cos \theta_0 (\hat{x} \sin \phi_0 - \hat{y} \cos \phi_0) \cdot \bar{\xi}_{t00} & q = 1 \\ \sec \theta_0 (\hat{x} \cos \phi_0 + \hat{y} \sin \phi_0) \cdot \bar{\xi}_{t00} & q = 2 \end{cases} \quad (52)$$

The solution of the resulting system of equations gives the vector of unknown coefficients  $\mathbf{E}$  in (1). The following section shows how these edge-field coefficients are used to find the transmission and reflection coefficients for the structure.

### 3.8. Transmissivity and Reflectivity

The most important quantities to be found from a periodic structure analysis are the surface transmissivity and surface reflectivity. These complex quantities provide knowledge of how the incident power divides itself between transmitted and reflected components, as well as the phase delay of the transmitted component.

The transmission coefficients for each mode are given by (33), since  $C_{pmn}^+$  represents the excitation of each mode propagating away from the array in the  $+z$  direction. However, when the transmission is into a different mode than the incident wave, such as in the case of grating lobes and Bragg lobes, the transmission coefficients need to take into account the differ-

ence in modal admittances. Letting  $\tau_{pmn}^+$  denote the transmission coefficient:

$$\tau_{pmn}^+ = \sum_{s \in \Gamma_{z^+}} e_s \sqrt{\frac{Y_{pmn}}{Y_{q00}}} \bar{\xi}_{smn}^* \cdot \bar{h}_{pmn} \quad (53)$$

The greatest interest is usually in the lowest order transmission coefficient in the  $m=n=0$  mode, especially when  $d_x, d_y \leq .5\lambda$ , in which case all higher order Floquet modes are evanescent. The lowest order transmission coefficient is the *transmissivity*, given by

$$\tau_{p00}^+ = \sum_{s \in \Gamma_{z^+}} \frac{e_s}{\sqrt{d_x d_y}} \bar{\xi}_{s00}^* \cdot \bar{\rho}_p \sqrt{\frac{Y_{p00}}{Y_{q00}}} \quad (54)$$

$$\bar{\rho}_p = \begin{cases} \hat{x} \sin \phi_0 - \hat{y} \cos \phi_0 & p = 1 \\ \hat{x} \cos \phi_0 + \hat{y} \sin \phi_0 & p = 2 \end{cases} \quad (55)$$

The modal reflection coefficients are found from (36). Except for the  $m=n=0$  mode, they are as given by (48) above, with  $\Gamma^-$  replacing  $\Gamma^+$ . The lowest order coefficient, the *reflectivity*, is

$$\tau_{p00}^- = \left[ \sum_{s \in \Gamma_{z^-}} \frac{e_s}{\sqrt{d_x d_y}} \bar{\xi}_{s00}^* \cdot \bar{\rho}_p - \delta_{pq} \right] \sqrt{\frac{Y_{p00}}{Y_{q00}}} \quad (56)$$

This concludes the presentation of the theory and formulation. The next chapter addresses various aspects of the implementation in a general-purpose computer code.

## 4. NUMERICAL IMPLEMENTATION

### 4.1. Geometry Generation

#### 4.1.1. CAD Geometry Definition

The finite element geometries are generated using a commercial "CAD" software package such as I-DEAS<sup>TM</sup> [15]. The objective is to create a numerical description of a complex geometry that the electromagnetic analysis code can interpret unambiguously. The general steps the user takes in the geometry generation process are:

1. Construct a wireframe geometry of points, lines and arcs
2. Use the curves (lines and arcs) to define surfaces
3. Group curves into mesh areas
4. Group mesh areas into mesh volumes
5. Generate the tetrahedral elements by subdividing mesh volumes
6. Tag elements (cells) with material properties
7. Tag nodes with boundary condition flags

Steps 1-5 are fairly generic, although the details may be peculiar to the particular software package used. Steps 6 and 7 will be described in further detail in sections 4.1.3 and 4.1.4.

#### 4.1.2. Unit Cell Side Wall Geometry Definition

A troublesome part of the periodic structure geometry generation is ensuring that the mesh on opposite unit cell faces lines up correctly. In order for the side wall periodicity condition to work, each side wall edge must have an identical "image" on the opposite side wall, with the same length and orientation. Each edge on the  $+x$  boundary must have an image on the  $-x$  boundary that has the same node coordinates except for a translation of  $(d_x, 0, 0)$ . Each edge on the  $+y$  boundary must have an image on the  $-y$  boundary that has the same node coordinates except for a translation of  $(d_x \cot \gamma, d_y, 0)$ . Figure 3 shows an example in which all of the geometry is blanked out except for the mesh on the unit cell perimeter, which is viewed from a point

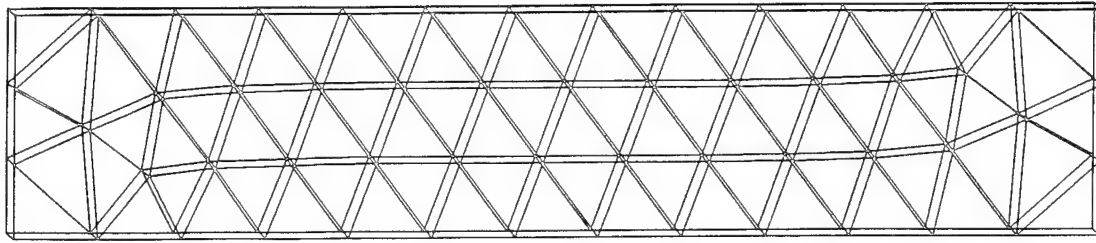


Figure 3. Side View of Example Mesh - Surface Grid on Unit Cell Walls Only

at a slight angle off the  $+x$  axis: The two sets of lines making up the side wall meshes overlay each other perfectly (only one set would be visible if it were viewed from a point on the  $x$  axis), which is the desired situation.

The I-DEAS<sup>TM</sup> software does not provide for achieving the result in Figure 3 directly. Instead, one must rely on the computer program's inherent repeatability. First, the lines that make up the unit cell outlines must be created with care to their *direction*, as indicated in Figure 4a. The mesh generation takes some of its cues on where to begin meshing an area by where lines begin and end. Hence, the lines that make up opposite side walls must have the same orientation. Next, the mesh areas that make up the unit cell perimeter must be defined first, before the top and bottom or any parts of the interior. This ensures that those areas will be meshed first, so the size and orientation of their triangular elements will not depend on interior details. Furthermore, the ordering of these mesh areas should be such that opposite walls are meshed sequentially, for example,  $-x$ ,  $+x$ ,  $-y$ , and  $+y$ . Finally, the curves making up opposite side wall mesh areas must be grouped in a consistent order. Figure 4b illustrates this by showing the order that curves are selected to make up the  $+x$  and  $-x$  side walls. These steps are

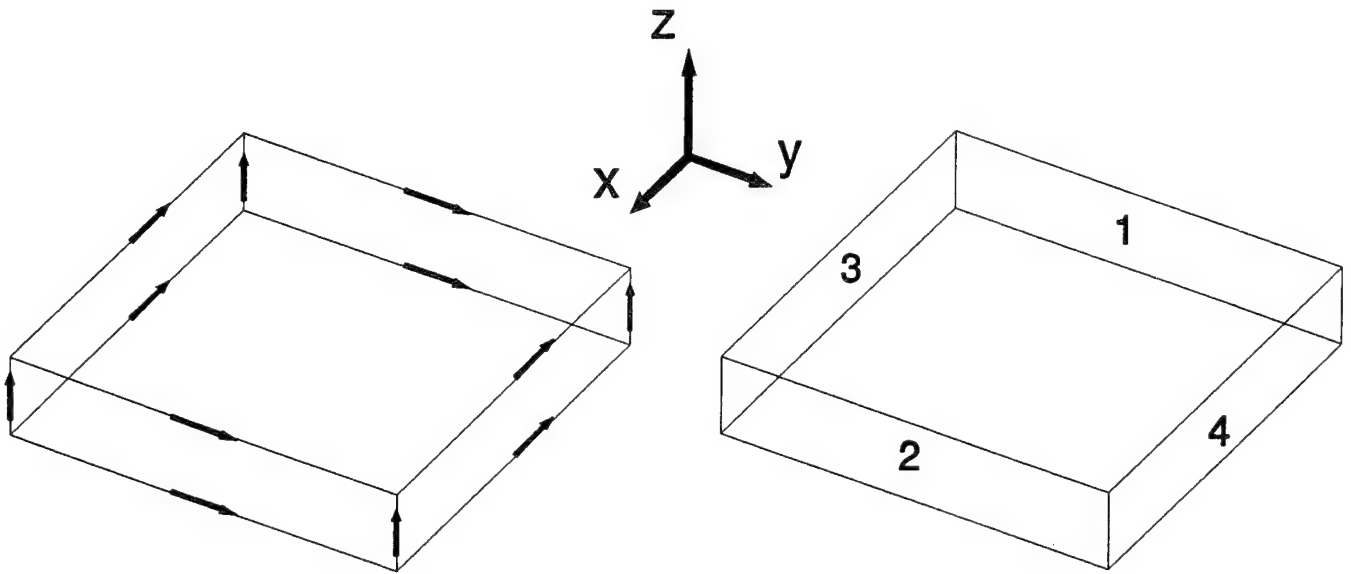


Figure 4. Direction and Sequence for Defining Curves and Mesh Areas to Achieve Identical Meshes on Opposing Unit Cell Side Walls: (a) Curve Directions; (b) Order of Selection for Curves to Make up Mesh Areas

generally adequate to ensure that I-DEAS<sup>TM</sup> will produce identical grids on opposite unit cell side walls.

#### 4.1.3. Conductor Boundary Conditions

There are various ways that any CAD package may be used to tag nodes in order to signal the electromagnetic code that they represent conductors. One easily-overlooked difficulty pertains to the way conducting boundaries are represented by the edge-based finite elements. If a mesh edge lies along a conductor, its tangential electric field must be zero. Therefore, there will not be any entries in the system of equations or in the matrix for those edges. However, there can be a field along an edge that joins two parts of the same conductor through free space or dielectric. Consequently, it is not adequate to simply tag all conductor nodes the same. The approach adopted in this work is to allow each node to belong to any or all of a range of con-

ducting surfaces, with a different tag for each. For example, the crossed dipole element in Figure 2 consists of two conductor groups: one for the horizontal arms; and another for the vertical arms. The nodes at the junction will belong to both groups. This allows the existence of a field component along diagonal edges joining vertical and horizontal arms near the junction.

#### 4.1.4. Node-Based to Edge-Based Geometry Conversion

Commercial CAD programs, usually geared toward mechanical engineering, generate geometry descriptions in terms of mesh nodes. Their typical output consists of a listing of node coordinates, then a listing of the node indices that define each element. The edge-based geometry adds a listing of edges by pairs of nodes. Another useful data structure is a listing of elements and the six edges that comprise each.

It is convenient, for this periodic structure problem, to order the edges so that those in the two radiation boundaries are first and last. As discussed in Section 2.2, this causes the two matrices associated with those boundaries to be zero except for dense upper left or lower right submatrices.

A crucial consideration is that the vector edge elements have direction. Throughout the matrix computations those directions must be accounted for. Referring to Eq. (6), the vector function is directed from the node  $i$  to the node  $j$ . A useful convention is to define the direction of an edge as being from the lower to the higher global node index.

While the matrix solution finds the field values along mesh edges, it is often useful to calculate the field at nodes. Node values are compatible with the commercial CAD software, which can be used to generate "rendered" plots of field lines or field contours superimposed on the geometry. The conversion procedure amounts to reconciling the two approximations

$$\bar{E} \approx \sum_{s=1}^{N_E} e_s \bar{\psi}_s \approx \sum_{t=1}^{N_N} \bar{e}_t f_t \quad (57)$$

where  $f_t$  is the conventional node-based finite element.

Consider the field within a single tetrahedron at a coordinate  $\bar{r}$ . If  $\bar{r}$  is much closer to node  $i$  than to any of the other three nodes  $j$ ,  $k$ , and  $l$ , the value of  $f_i$  is nearly unity, while  $f_j$ ,  $f_k$ , and  $f_l$  are nearly zero. Then the nodal approximation to the field is

$$\bar{E}(\bar{r}) \approx \bar{e}_i f_i \quad (58)$$

The field due to the edge expansion is almost entirely due to the three edges leading into node  $i$  since that of the three opposing edges depends only on  $f_j$ ,  $f_k$ , and  $f_l$ :

$$\bar{E}(\bar{r}) \approx L_{ij} e_{ij} f_i \nabla f_j + L_{ik} e_{ik} f_i \nabla f_k + L_{il} e_{il} f_i \nabla f_l \quad (59)$$

Equating (58) and (59) gives

$$\bar{e}_i \approx L_{ij} e_{ij} \nabla f_j + L_{ik} e_{ik} \nabla f_k + L_{il} e_{il} \nabla f_l \quad (60)$$

Due to the piecewise linear nature of the approximation for the electric field, the right hand side of (60) may be slightly different within each cell bordering on the node, so the conversion procedure takes the average over all cells adjacent to the node.

#### 4.2. Matrix Data Structure and Computations

To take advantage of the matrix sparsity, an iterative solution is anticipated. This is as much for reasons of storage as for solve time. An enormous savings in computer memory can be realized by storing only the nonzero matrix elements. However, a "direct" solver, based on Gaussian elimination (usually LU decomposition) creates new elements as the solution proceeds,



so that the LU factors are less sparse than the original matrix. Iterative solvers such as the conjugate gradient method (CGM) [16] and biconjugate gradient method (BCGM) [17], discussed further in Section 4.3, operate by making successive guesses at the solution vector, always using the original matrix. Therefore, they require minimum storage. They also usually require less execution time than ordinary LU decomposition.

Based on the above rationale, the data structure employed in this solution used three separate arrays. The two radiation boundaries are represented by storing the dense upper left or lower right submatrix in a two-dimensional array. The sparse interior matrix entries are stored as a one-dimensional array, with two integer arrays giving the row and column index of each entry. Of course, there are sparse matrix storage schemes that get by with only one integer array [18]. However, it is most convenient to execute the finite element computations one *cell* at a time, rather than one edge at a time. The matrix entries for edge pairs are created in whatever order those pairs are first encountered when stepping through the cells.

### 4.3. Matrix Solution

Two separate iterative matrix solvers were implemented and tested as part of this work. The first is the conjugate gradient method (CGM). It did not fail to converge during any of the validation cases attempted. The second solver, the biconjugate gradient method (BCGM), usually converged much faster than CGM. However, there were several cases for which it did not converge at all, most notably resonant-element FSSs at frequencies near resonance.

#### 4.3.1. Conjugate Gradient Method

The essential CGM algorithm is given by Sarkar and Arvas [16]. The procedure to solve  $AX = B$  for the unknown vector  $X$  begins with an initial guess  $X_0$ , giving an initial residual error

vector  $R_0 = B - AX_0$ . The initial search direction and gradient vectors  $P_0$  and  $G_0$  are

$$P_0 = G_0 = A^H R_0 \quad (61)$$

(The superscript H denotes Hermitian, that is, conjugate transpose.) The iteration consists of the following steps using  $\| \cdot \|$  to denote the  $L_2$  norm:

$$\alpha_i = \frac{\|G_i\|^2}{\|A P_i\|^2} \quad (62)$$

$$X_{i+1} = X_i + \alpha_i P_i \quad (63)$$

$$R_{i+1} = R_i - \alpha_i A P_i \quad (64)$$

$$G_{i+1} = A^H R_{i+1} \quad (65)$$

$$\beta_i = \frac{\|G_{i+1}\|^2}{\|G_i\|^2} \quad (66)$$

$$P_{i+1} = G_{i+1} + \beta_i P_i \quad (67)$$

A typical convergence test is to examine the ratio  $\epsilon = (\|R_i\|^2 / \|R_0\|^2)$  at each iteration. A value of  $10^{-3}$  or  $10^{-4}$  is usually adequate to ensure convergence of the transmissivity and reflectivity. Figure 5 shows the convergence of the reflectivity from a single layer of spherical conductors in a square lattice (discussed later in Section 5.3), along with the convergence of the residual norm. Both of these quantities are converging monotonically.

#### 4.3.2. Biconjugate Gradient Method

The generalized biconjugate gradient method requires an additional two  $1 \times N$  complex

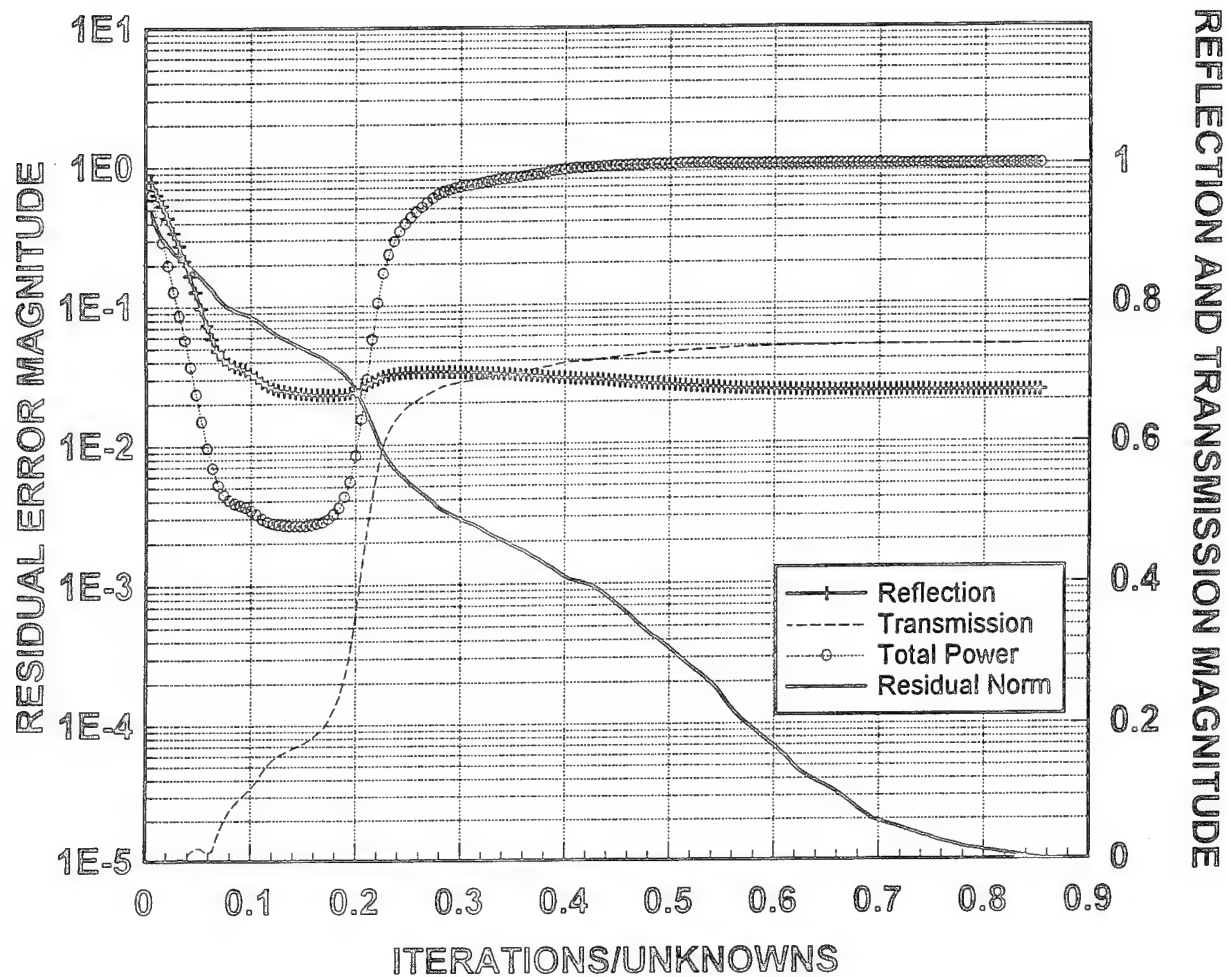


Figure 5. Convergence of Residual Norm, Reflectivity and Transmissivity using Conjugate Gradient Method

arrays for storage, which is usually tolerable. The search algorithm begins with the following initial conditions [17]:

$$X_0 = 0 \quad (68)$$

$$R_0 = P_0 = B \quad (69)$$

$$W_0 = Q_0 = B^* \quad (70)$$

The vectors  $W$  and  $Q$  are in addition to  $R$  and  $P$ , which were required by the CGM. The

following steps comprise the iteration procedure:

$$\alpha_i = \frac{\langle R_i, Q_i \rangle}{\langle A P_i, W_i \rangle} \quad (71)$$

$$X_{i+1} = X_i + \alpha_i P_i \quad (72)$$

$$R_{i+1} = R_i - \alpha_i A P_i \quad (73)$$

$$Q_{i+1} = Q_i - \alpha_i^* A^H W_i \quad (74)$$

$$P_{i+1} = R_{i+1} + \beta_i P_i \quad (75)$$

$$W_{i+1} = Q_{i+1} + \beta_i^* W_i \quad (76)$$

$$W_{i+1} = Q_{i+1} + \beta_i^* W_i \quad (77)$$

where  $\langle \cdot, \cdot \rangle$  denotes the inner product of two vectors. Figure 6 shows the convergence of the residual norm for the same test case as Figure 5. Unlike CGM, the residual norm does not converge monotonically, or even gradually. Nonetheless, BCGM required less than .2N (N is the number of unknowns) iterations to converge in this case, whereas CGM required 1.8N.

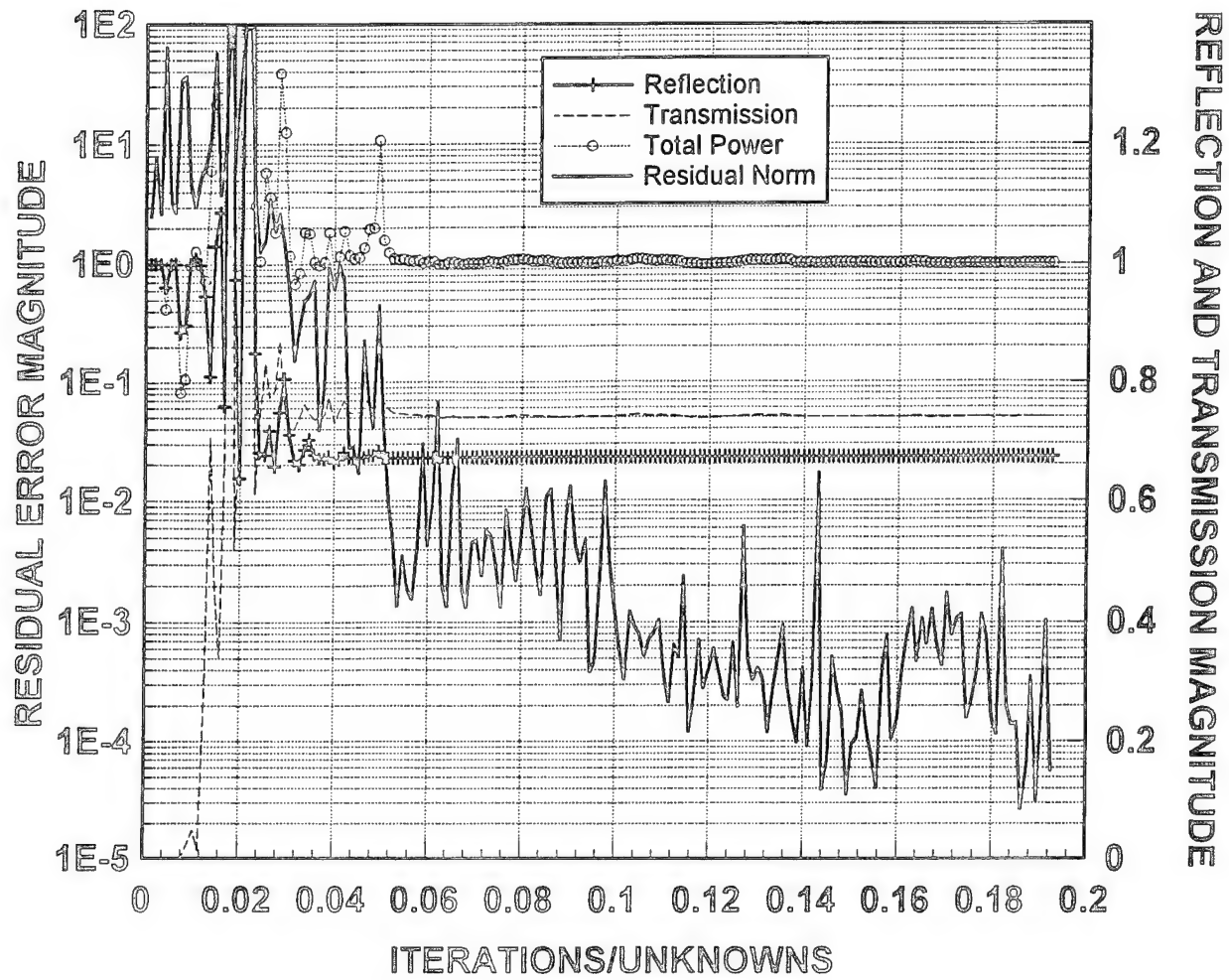


Figure 6. Convergence of Residual Norm, Reflectivity and Transmissivity using Biconjugate Gradient Method

## 5. VALIDATION

The theory presented in Chapter 3, and the code design presented in Chapter 4, were validated by comparing the code results for several test cases to analytical formulas, measurements, or calculations made with other, fundamentally different methods. These results serve to show that the new technique is accurate, flexible and dependable. These test cases were: (1) a dual-layer inductive screen filter; (2) a wire grid array; (3) an artificial dielectric made of conducting spheres; (4) a band-stop filter made of layered dielectric rods; (5) a lattice of crossed conductor bars in a dielectric slab, emulating reinforced concrete; and (6) a crossed-dipole FSS. The last section in this Chapter compares the computational effort required in terms of both storage and execution time.

### 5.1. Inductive Screen Filter

The crossed conducting grid shown in Figure 7 is an inductive screen. (Its electromagnetic "dual," conducting patches, would be a capacitive screen.) It functions as a high-pass filter, reflecting most of the energy below the frequency at which the aperture spacing is one wavelength. Combining two or more screens in series sharpens the frequency rejection, by forming a cascaded, two-pole filter.

Lee et. al. solved for the transmission characteristics of these screens using the *mode matching* method [19]. This method expands the fields in a series of plane wave modes (Floquet modes) [20]. It is a form of moment method in the sense that it is a matrix solution to a frequency-domain integral equation. The expansion and testing functions are the plane wave modes themselves (entire domain functions).

Figure 8 shows the representation of one unit cell of this structure by a tetrahedron mesh.

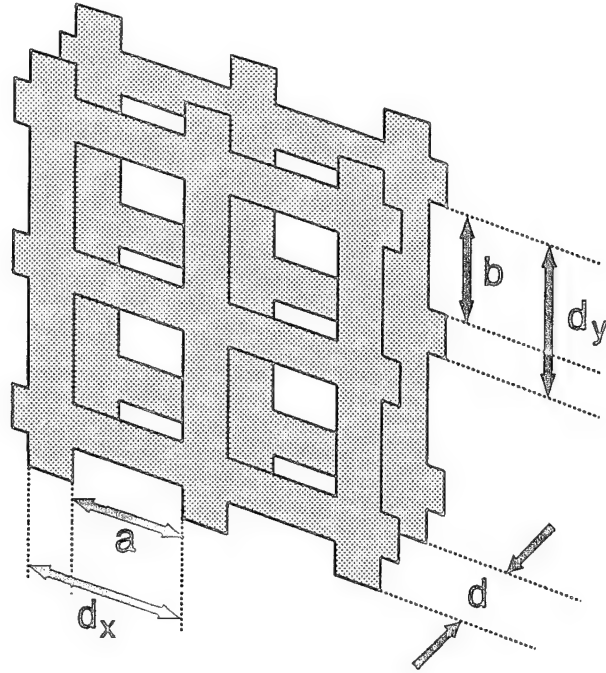


Figure 7. Two-Layer Inductive Screen

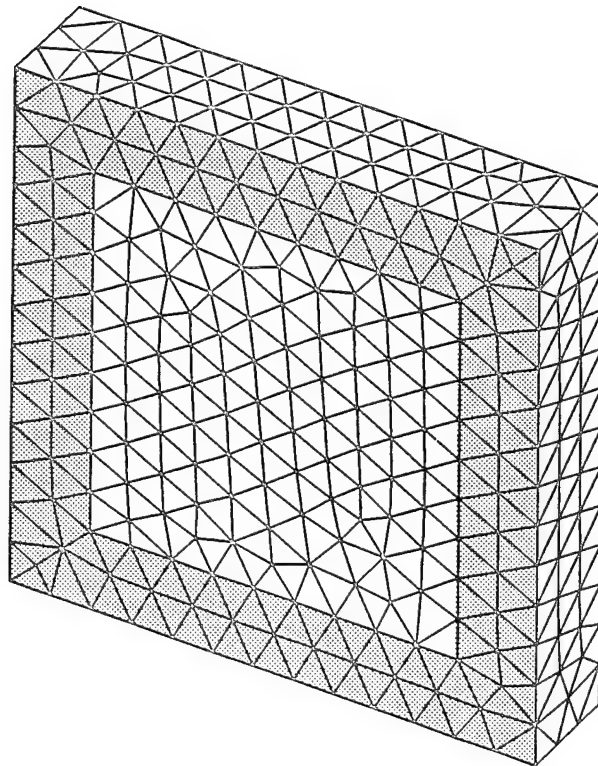


Figure 8. Tetrahedron Mesh for a Unit Cell of the Two-layer Inductive Screen

The shaded areas indicate those cell faces that are defined as perfect conductor. The mesh density is approximately 13 cells per wavelength at the highest frequency, which corresponded to a unit cell width and height of one wavelength. For this test case, the spacing between screens was  $d=.2a$  and the aperture size was  $a=b=.7d_x=.7d_y$ .

Figure 9 shows the calculated power transmission through the double screen. The agreement between the HFEM code and the moment method calculations from [19] is excellent. This provided an initial validation of several features of the theory, such as the periodic radiation condition, the side-wall periodicity conditions, and the interior finite element calculations. In short, these results could not have been obtained if there were any errors in the theory or implementation of the matrix equation derived in Chapter 3. It also verifies the correctness of the formulation for the forcing function due to the incident field, and the subsequent calculation

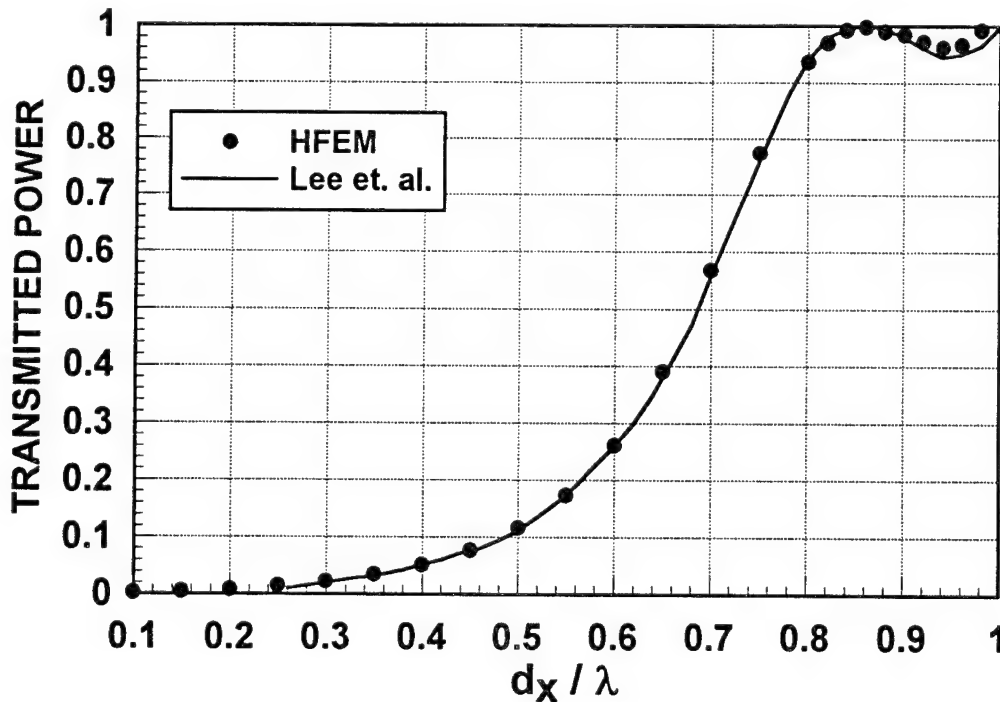


Figure 9. Comparison of HFEM and Method of Moments [19] Calculations for Transmission through Two-Layer Inductive Screen:  $d_x=d_y$ ,  $a=b=.7d_x$ ,  $d=.2a$



of transmissivity from the electric field solution.

This test case also illustrates that the FEM does not have any difficulty with sharp conducting edges, and does not require extraordinarily high grid resolution near such edges. It also serves to illustrate that the outer surfaces of the material structure, conducting surfaces in particular, may coincide with the radiation boundary. Hence, it is not necessary to add any grid cells in free space above or below the structure.

## 5.2. Wire Grid Array

As mentioned earlier, wire grids can be used as angular filters to reduce the sidelobes of an antenna. In addition, linearly polarized reflector antennas are often constructed from parallel wires or bars in order to reduce weight and wind resistance. To properly design such an antenna, it is necessary to know how closely the wires must be spaced to provide good reflection at all incidence angles.

Decker performed measurements of transmission through a wire grid as a function of angle, with the incident electric field polarized parallel to the wires [21]. He compared those measurements to analytical formulas from Wait [22].

To use the hybrid finite element method for this calculation, the grid shown in Figure 10 was used. The short section of wire is represented as a void in the tetrahedron mesh, indicated by the shaded area. The grid is fairly wide in the  $x$  dimension, corresponding to the spacing between wires (1.5 cm). The wire radius is 1 mm.

Figure 11 compares the HFEM results with those given by Decker, both measured and calculated ( $f=9.6$  GHz). The HFEM calculations are somewhat closer to the measured data, most notably at normal incidence. The discrepancy between the measurement and both sets of

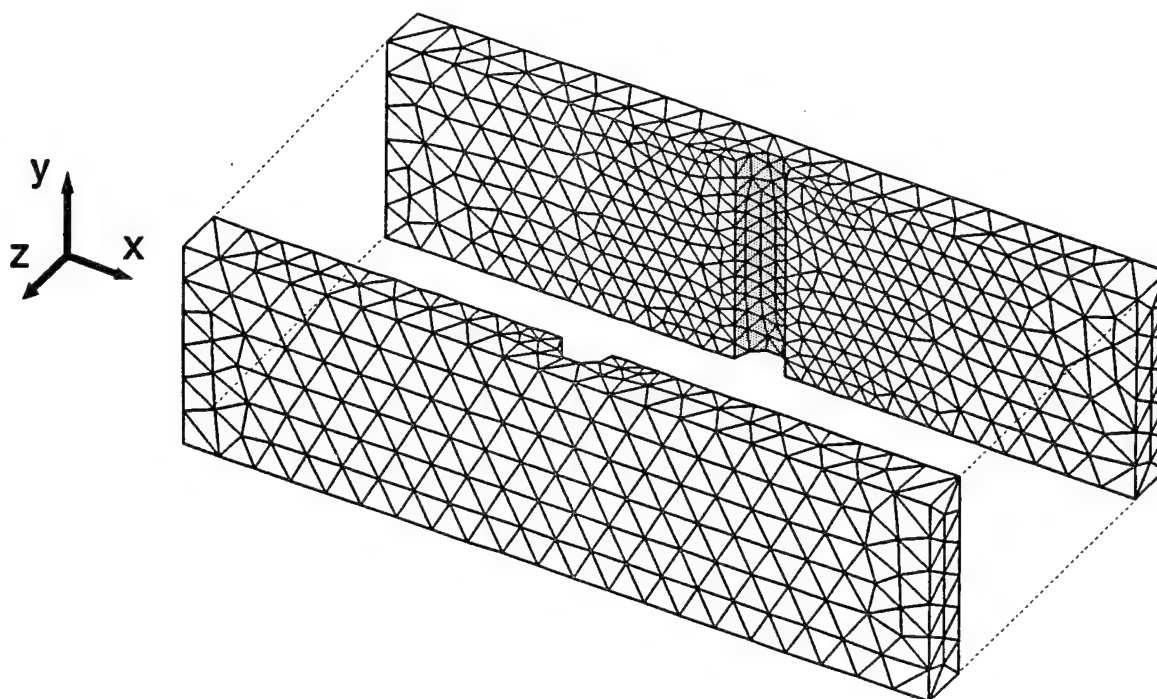


Figure 10. Tetrahedron Mesh for Wire Grid Array

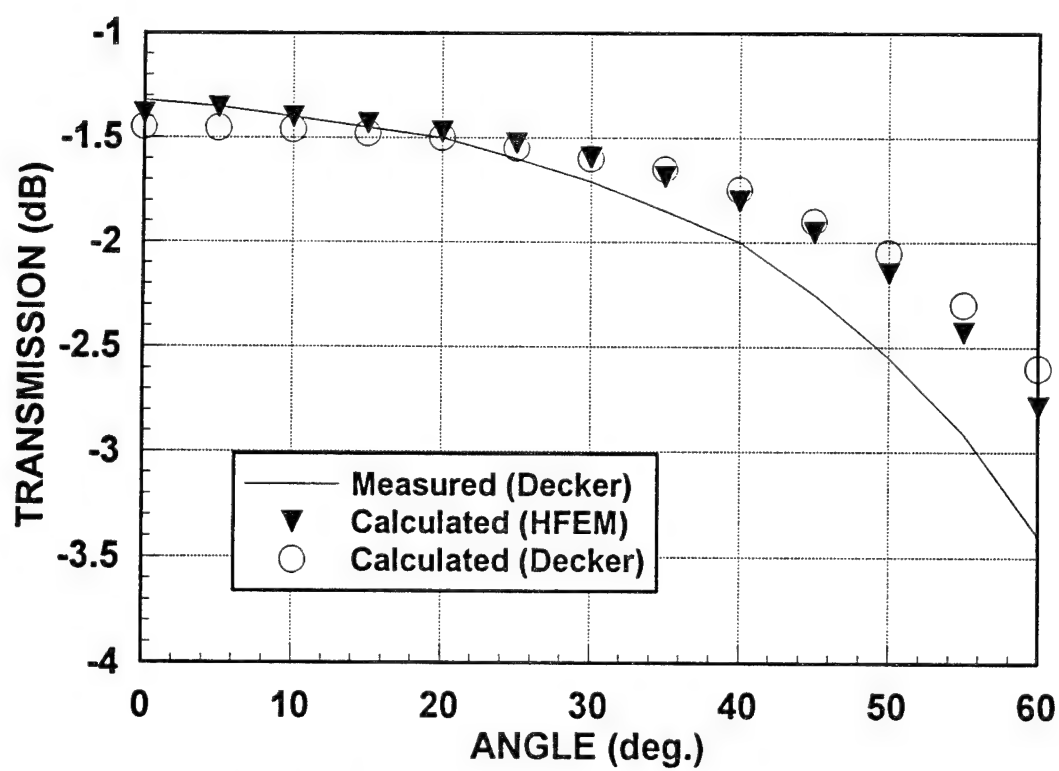


Figure 11. Parallel-polarized Transmission through Wire Grid Array vs. Scan Angle

calculations at wide angles is most likely due to the fact that the test article was fairly small in both width and length, allowing for diffractions from its edges.

It is, of course, quite inefficient to use a three-dimensional code for this inherently two-dimension problem. However, it serves to illustrate that the HFEM code correctly models situations in which infinite conductors are represented as objects projecting through opposite unit cell walls. A later section presents a similar case in which wires (or bars) continue through opposite unit cell faces in both directions, representing a grid of crossed wires.

### 5.3. Artificial Dielectric

Artificial dielectrics are synthetic delay media made up of dielectric or metallic obstacles imbedded in a natural-dielectric medium, or binder. The obstacles are usually arranged in a regular lattice and are individually much smaller than the wavelength at which the structure is intended to function. Artificial dielectrics have the advantage that they may have refractive indices that are much higher, for a given weight, than natural dielectrics.

One such medium is an array of metal spheres. When arranged in a cubic lattice, the effective permittivity, permeability, and index of refraction may be estimated analytically using conformal transformations. Lewin derived the following expressions [23]:

$$\epsilon_r = \epsilon_{rd} \frac{1 + 2g}{1 - g} \quad (78)$$

$$\mu_r = \frac{1 - g}{1 + g/2} \quad (79)$$

$$g = \frac{\pi D^3}{6V} \left[ 1 - 12.96 (D/\lambda_d)^2 \right]^{-1} \quad (80)$$

where  $\epsilon_{rd}$  is the relative permittivity of the binder material,  $\lambda_d$  is the wavelength in the binder,  $D$  is the sphere diameter, and  $V$  is the unit cell volume. These formulas are expected to be valid for  $D/\lambda_d \leq .2$  [4]. From (78) and (79), the effective index of refraction is

$$n = \left[ \epsilon_{rd} \frac{1 + 2g}{1 + g/2} \right]^{1/2} \quad (81)$$

The phase delay (in deg.) through a layer of thickness  $t$  is

$$\Delta \phi = \frac{360 n t}{\lambda_{rd}} \quad (82)$$

Figure 12 shows a tetrahedron mesh of the air space surrounding a metal sphere. The sphere diameter is 2 m, and the cube is 4 m on each side, so that  $V = 64 \text{ m}^3$ . Since the sphere is an impenetrable conductor, it is represented as a void in the mesh.

The formulas (78)-(82) apply to a uniform, infinite medium. However, the calculations are for a structure with finite thickness. Therefore, it will include edge effects at the surface

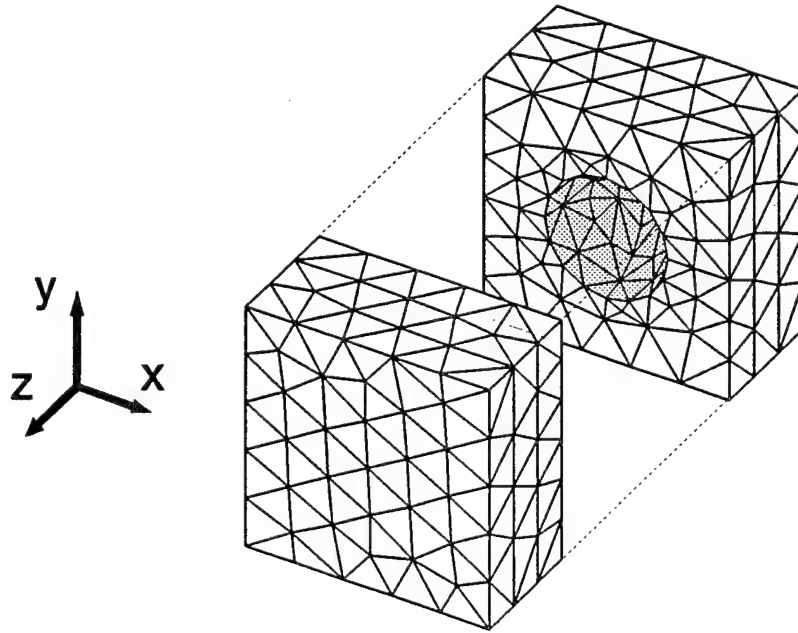


Figure 12. Tetrahedron Mesh for a Conducting Sphere in a Cubic Lattice

that are not accounted for by the analytical model. To make a comparison, three separate FEM models were used, consisting of 3, 4 and 5 layers of spheres, with layers separated by 4 m. The differential transmission phase from (82) for a single layer is plotted as the solid line in Figure 13. The abscissa corresponds to increasing frequency with a fixed cell size. The discrete points are the difference in transmission phase computed by HFEM with 3 and 4 layers (triangles) and 4 and 5 layers (circles). It is evident that as more layers are added, the calculations become closer to the analytical formulas. The formulas are not accurate for  $D/\lambda_d > .2$ , corresponding to  $d_x/\lambda_d > .4$ , so the disagreement at the higher frequencies is expected.

#### 5.4. Dielectric Bandgap Structure

Photonic bandgap structures are crystals in which certain photon energy states are forbidden. They have been proposed as a means for improving the quantum efficiency of lasers [24].

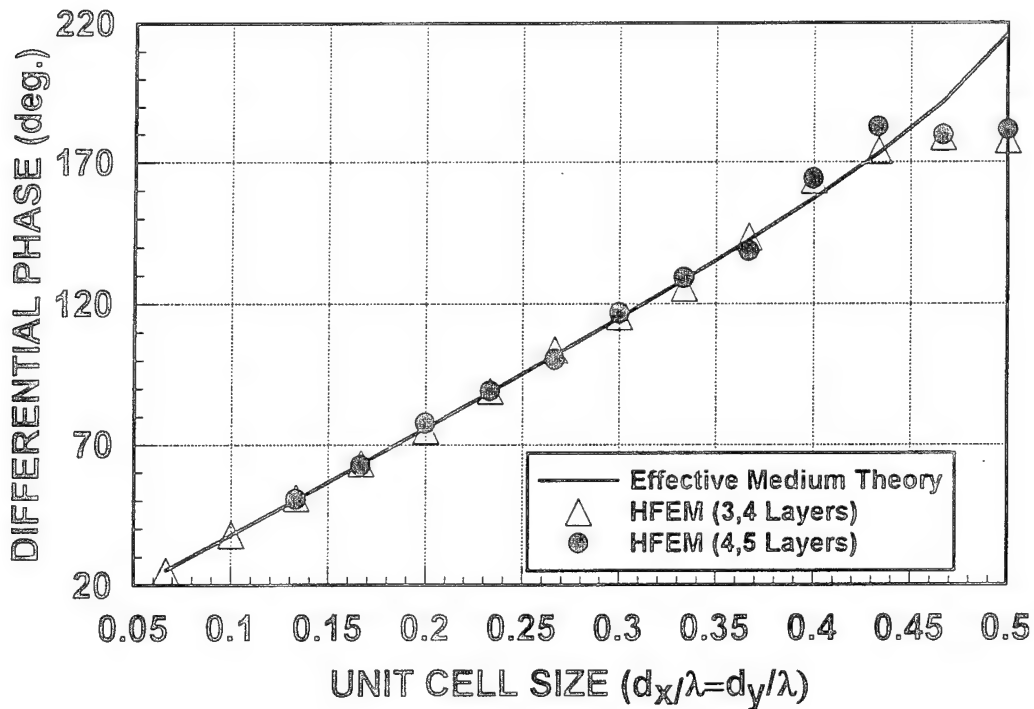


Figure 13. Differential Transmission Phase for a Single Layer of Artificial Dielectric

There is a direct analogy between the quantum states in a crystal and microwave frequencies in a (much larger) scaled lattice of dielectric obstacles or voids in a solid dielectric [25]. The dielectric structure will have a frequency stop band corresponding to the photonic band gap.

An example bandgap structure is an array of layered dielectric rods. Figure 14 shows the cross sectional geometry of one rod in an array whose transmissivity was measured by Kelly et. al. [26]. The array was up to ten layers of these rods in a 12.7 mm x 12.7 mm square lattice. The acrylic tubes have relative permittivity  $\epsilon_r=2.55$  and inner and outer radii of  $b = 3.175$  mm and  $c = 4.763$  mm. Each may have a pyrex core with radius  $a = 3.0$  mm and  $\epsilon_r=4.2$ . There is a small air gap between the pyrex core and the acrylic sheath. In Kelly's measurements, seven of the rows had pyrex cores and the last three had the acrylic tubes only.

For purposes of the finite element calculations, the air gap is ignored and the acrylic tube is assumed to have an inner diameter of 6.0 mm. The tetrahedron mesh for a single rod is shown exploded in Figure 15a. Note that since pyrex has a refractive index of approximately 2, the mesh in that material is twice as dense as in the air region. Figure 15b shows the unit cell mesh for a four-layer structure. Only the very narrow end of the mesh is subject to the

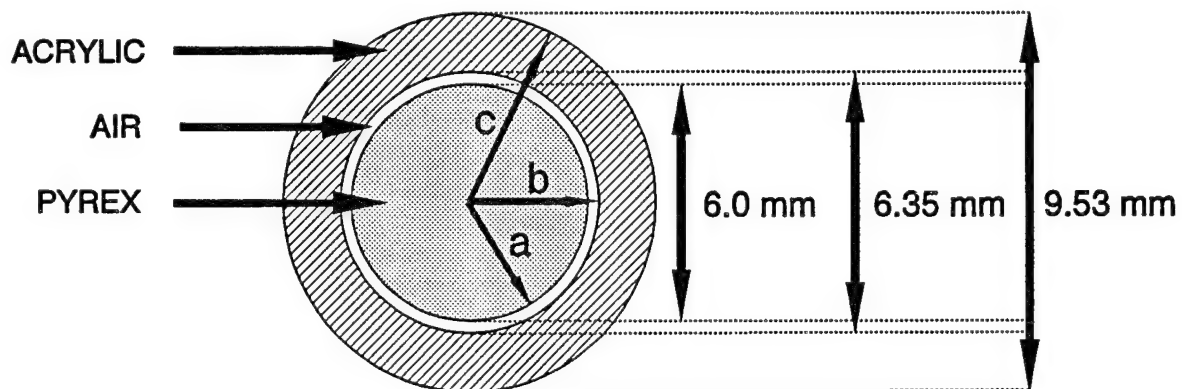


Figure 14. Layered Dielectric Rod used to Simulate Photonic Band Structure

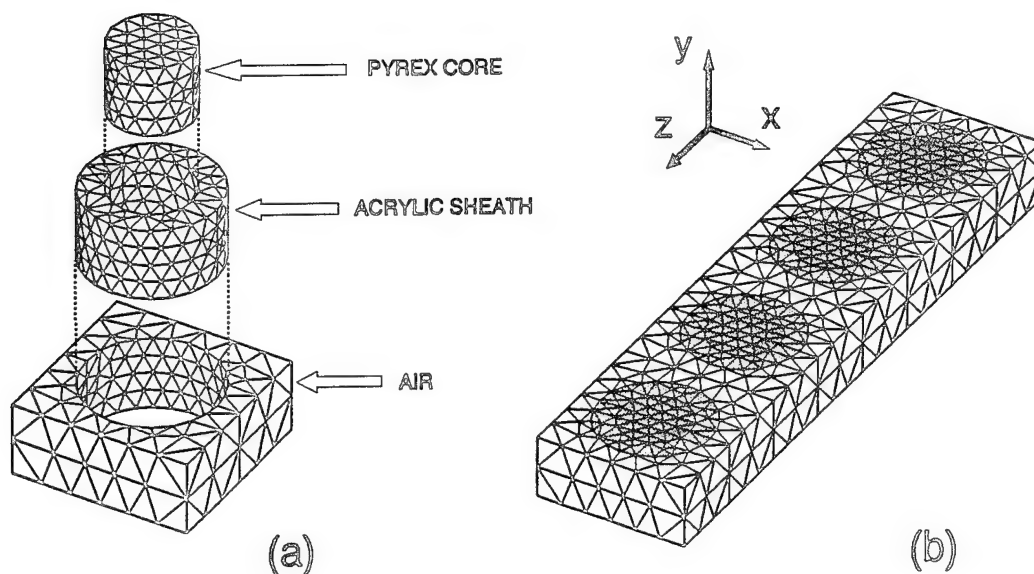


Figure 15. Tetrahedron Mesh for Layered Dielectric Rods: (a) Exploded View of Single Rod; (b) Unit Cell Mesh for Four-layer Structure

incident field and periodic radiation conditions.

Figure 16 is a comparison between the HFEM calculations and the measurements for the case in which the incident electric field is aligned parallel to the rods. The calculations reveal quite clearly the presence of a stop band in the region from 7 GHz to 10 GHz, which was predicted by plane wave theory [26],[27]. The measurements only go down to -20 dB transmissivity in the stop band for either or both of two reasons: (1) the structure measured was fairly small in width and height, which is not truly representative of an infinite structure; or (2) the measurement antennas were fairly close to the structure's surfaces, so that the incident and transmitted fields were not representative of plane waves.

As was the case with the wire grid array, this lattice of rods is inherently a two-dimensional problem. Hence it is inefficient to model it with a 3-dimensional code, unless the transmission and reflection at arbitrary incidence angles and polarizations is important. However,

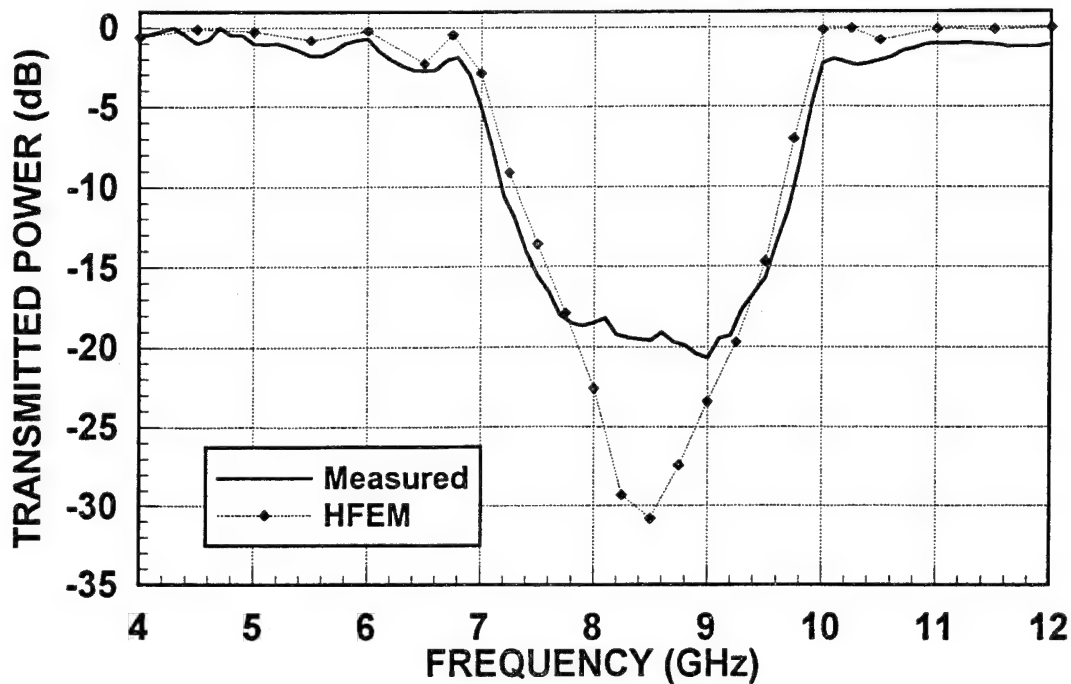


Figure 16. Comparison of Hybrid Finite Element Method Calculations and Measurements for 10-layer Dielectric Rod Array

the most interesting photonic band structures are crystal lattices, which cannot be represented as 2-dimensional structures. The hybrid finite element method clearly has the capability of dealing with general 3-dimensional bandgap structures, and the potential to supplant tedious and expensive measurements.

### 5.5. Reinforced Concrete

Reinforced concrete walls are usually made up of regular lattices of steel reinforcing bars in the center of the concrete layer. Their level of protection from radio frequency energy, or *shielding effectiveness*, has much more to do with the reinforcing bars than the concrete itself. There is tremendous variation in the electrical properties of concrete, depending mainly on its water content, but it does not usually attenuate RF energy very well by itself. Hence, predicting the shielding effectiveness of reinforced structures depends on being able to predict the trans-



missivity of the reinforcing lattice. This test case assumes a lattice of reinforcing bars with 4" spacings in both directions, and 1/8" bar diameter. The effect of the spacing between bars will be shown to make a difference under some conditions of incidence angle and polarization.

Figure 17 shows one half of the tetrahedron mesh representation for a single unit cell with 1/8" spacing between the vertical and horizontal bars. Again, the conductor interiors are represented as voids in the mesh. The maximum mesh edge length is .4", so that it is valid for frequencies up to 3 GHz. The edge length is smaller in the vicinity of the bars to ensure that there is no more than 20% deviation from the actual surface curvature. The surrounding cells may be assigned any value of complex permittivity. For these calculations, the permittivity was set to (1.0,0.0), representing air. The effect of a real permittivity greater than 1 will be to shift the results down in frequency. The effect of an imaginary part greater than 0 will be to reduce the transmitted power. A second mesh, not shown, models a case in which the horizontal and vertical bars just touch each other at a single point.

Figure 18 compares two sets of calculations for the two cases for normal incidence. Evidently, when the wave is polarized parallel to either set of bars, the transmissivity is the same whether or not they are electrically connected. However, for oblique incidence, the situation is quite different, as Figure 19 attests. Here, the wave is incident from  $(\theta_0, \phi_0) = (30^\circ, 45^\circ)$ , with transverse electric polarization (electric field polarized  $45^\circ$  to both sets of bars). When the bars are connected, circulating currents are induced that create a resonance condition near 1.75 GHz, with zero co-polarized transmission. (There is a small amount of power transmitted in the orthogonal polarization.) This transmission null will shift in frequency as the incidence angle changes. Both curves indicate a drop in transmissivity above 2.25 GHz, but that is due to the fact that the transmitted power is split between the main lobe and a grating

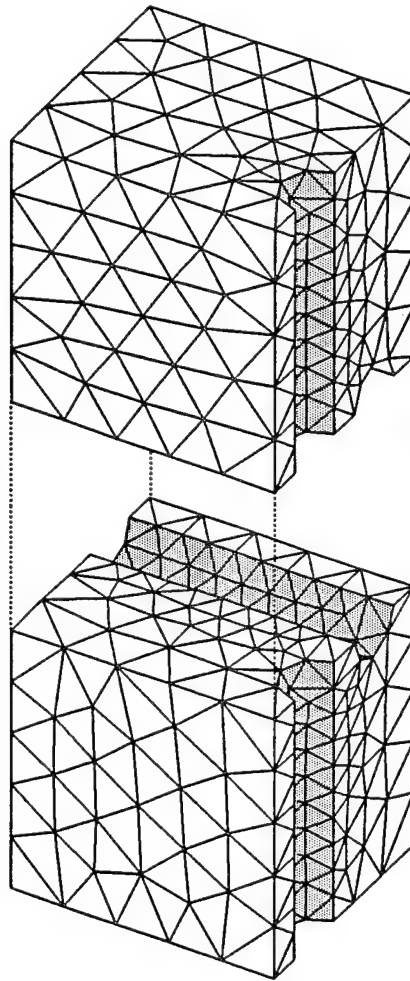


Figure 17. Cutaway of One Half of Tetrahedron Mesh for Reinforced Concrete Unit Cell

lobe. The grating lobe power is not accounted for in this calculation. The total transmissivity, including the grating lobe, will be near unity above 2.25 GHz.

### 5.6. Crossed Dipole Frequency Selective Surface

The crossed dipole FSS illustrated in Figure 2 is the only test case attempted so far for which satisfactory results have not yet been obtained. The crossed dipole array was an early attempt at a "dichroic" surface that would reflect a single frequency and pass all others. The intended use was a subreflector for a large parabolic dish. The subreflector would pass energy

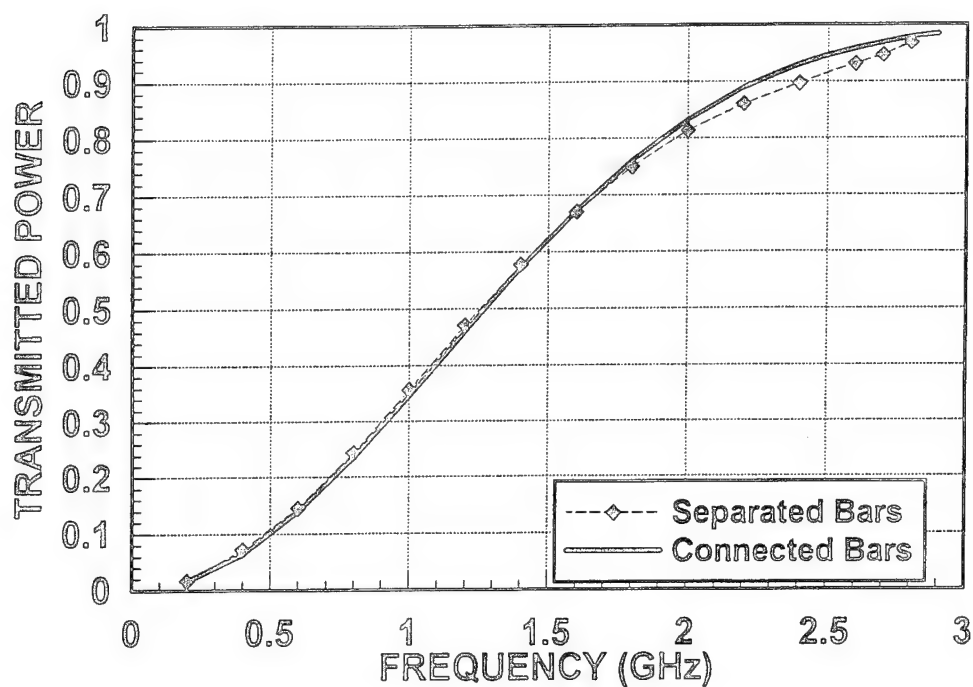


Figure 18. Normal-incidence Transmission through 4"x4" Reinforcing Bar Lattice

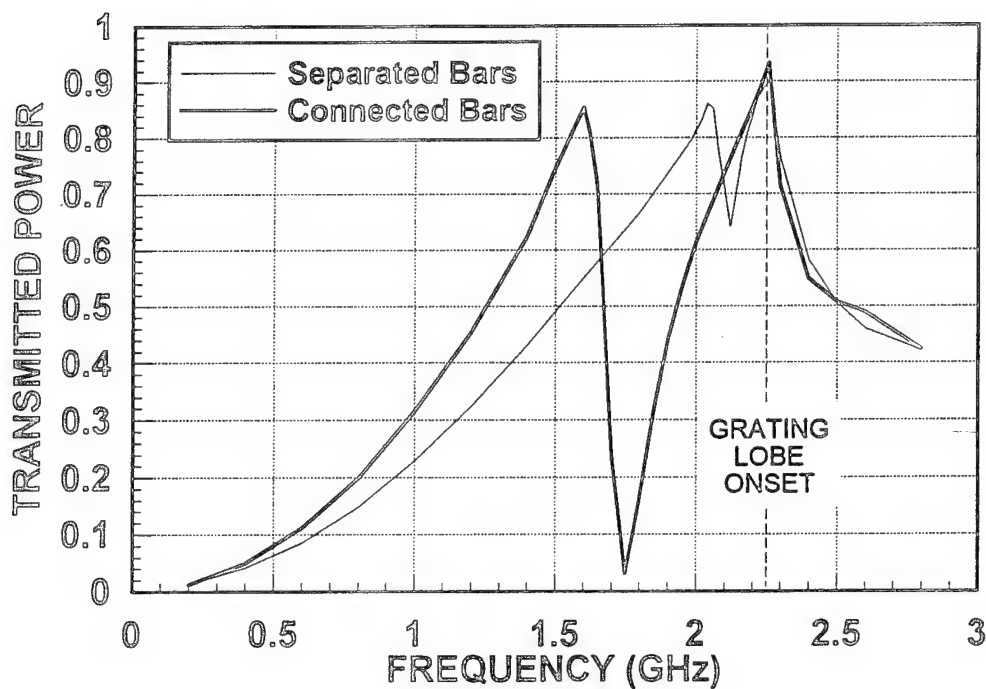


Figure 19. Oblique-incidence Transmission through 4"x4" Reinforcing Bar Lattice:  
 $(\theta_0, \phi_0) = (30^\circ, 45^\circ)$ , Transverse Electric Polarization

from a feed located at the dish's focus, while reflecting that from a feed located in the center of the dish. Unfortunately, the crossed dipole element was deficient because at off broadside scan angles it has an anti-resonance, sometimes called a "Wood's anomaly" [28]. Figure 20 shows the element and lattice dimensions and the unit cell outline. Figure 21 compares the HFEM calculations with method of moment results from Cwik & Mittra [29]. The effect observed when attempting this problem with HFEM is a shift in the resonant frequency and a broadening of the frequency response. The grid used for the HFEM results is shown in Figure 22, which includes two air layers on each side of the dipole elements. The grid had a mesh edge length less than  $\lambda/30$  in the plane of the dipoles at the frequency where the anti-resonance occurs. Even though that would ordinarily be an excessively fine mesh, it is evidently not fine enough in this case. Accurate results for such cases may require the development of special singularity finite elements. Although such elements are common in mechanical engineering applications, they are only beginning to see development for electromagnetic problems.

### 5.7. Storage, Execution Time and Accuracy Issues

Table I shows the sizes of each of the test cases in terms of the mesh sizes and storage required. In all cases, the storage needed for the matrix, both sparse and dense parts, is less than 4 Mb (Megabytes) using single-precision complex representation (8 bytes per number, or "word"). The total number of mesh edges is almost always less than 1.5 times the number of mesh cells. For the sparse matrix,  $S^I$ , there are typically 15 or less entries per matrix row. The number of edges in the two radiation boundaries is always less than  $8 \cdot d_x \cdot d_y / \ell^2$ , where  $\ell$  is the mesh edge length. An exception is when part of the radiation boundary is filled with conducting surfaces, as in the case of the inductive grid (see Fig. 8). In summary, the storage required for

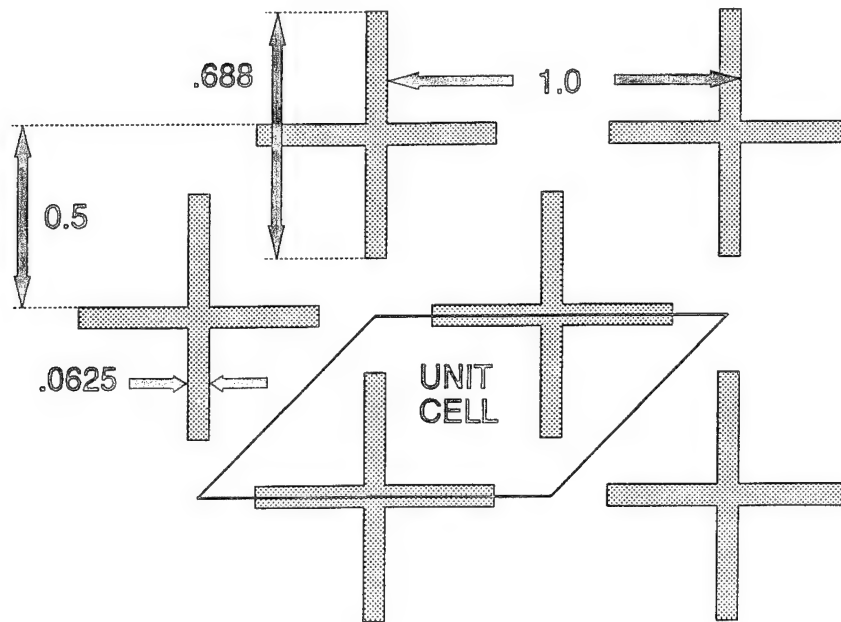


Figure 20. Crossed Dipole FSS Element and Lattice Geometry

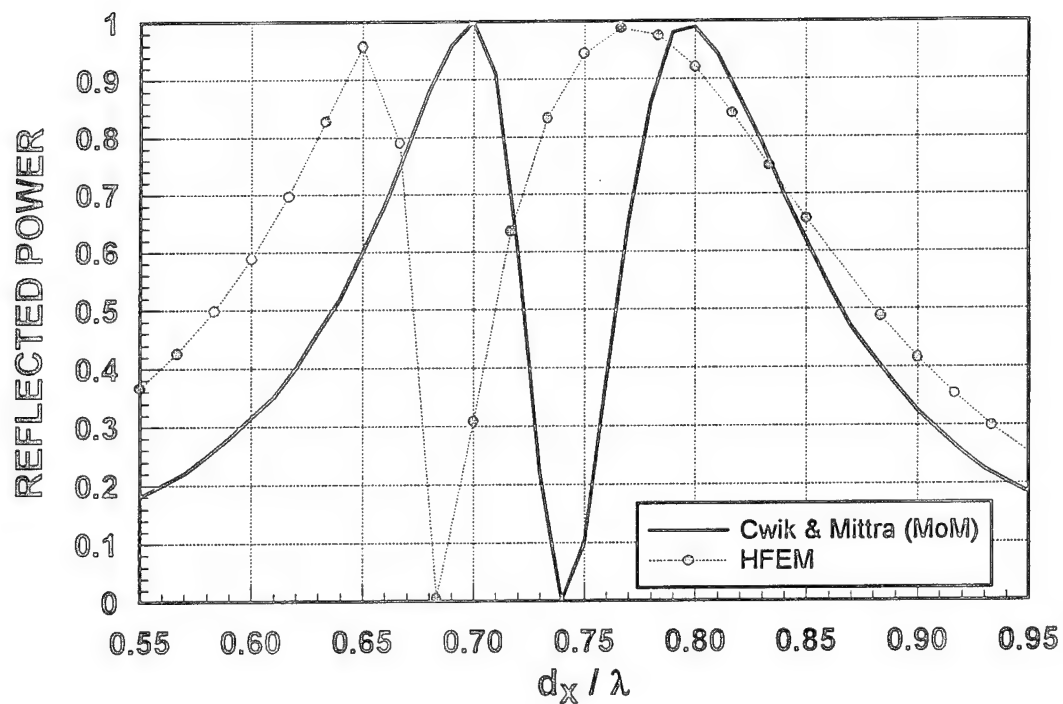


Figure 21. Comparison of HFEM and MoM Calculations of TM Reflection from Crossed Dipole Frequency Selective Surface ( $\theta_0=30^\circ, \phi_0=0^\circ$ )

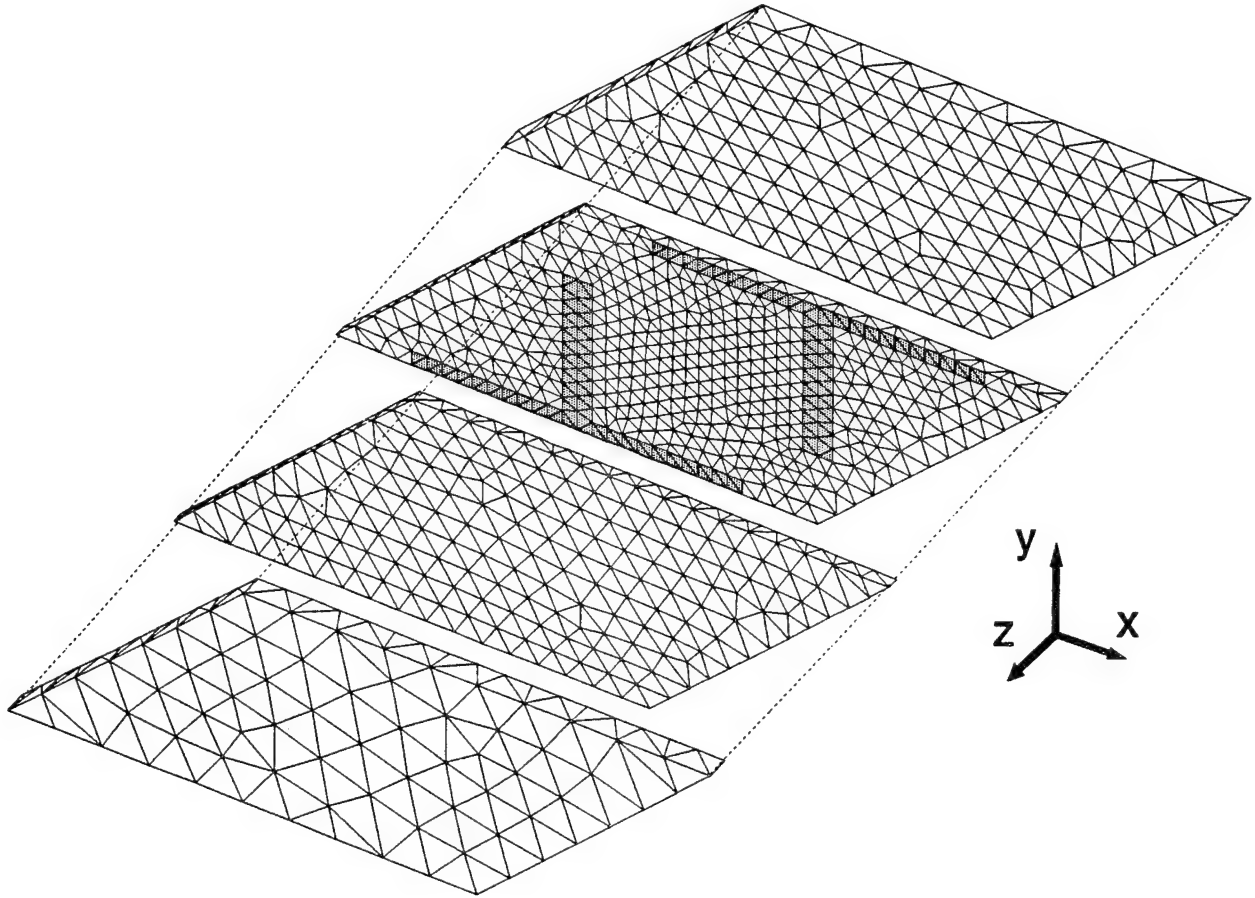


Figure 22. Tetrahedron Mesh for Crossed Dipole Frequency Selective Surface  
Test Case: Two Air Layers Surround the Conducting Elements

any problem may be estimated *a priori* as

$$\text{Matrix Storage (words)} < (15)(1.5) N_c + (8) \frac{d_x d_y}{l^2} \quad (83)$$

where  $N_c$  is the number of mesh cells.

Table II summarizes the execution time for each case using a SparcStation<sup>TM</sup>-20 computer. These are averages over all of the frequencies or angles for which results were shown in the previous sections. Each new angle or frequency requires a separate matrix fill and solve. It is immediately apparent that the biconjugate gradient solver has a distinct advantage, converg-

Table I. Mesh Sizes and Storage Requirements for Test Cases

TEST CASE	Cells	Edges	Edges in $\Gamma_z, \Gamma_{z+}$	Matrix Entries per Row	$d_x d_y / \ell^2$	Matrix Storage (MB)
Inductive Screen	1827	2244	290	13	81	.57
Wire Grid Array	5517	7030	816	14.7	122	3.49
Artificial Dielectric						
3 Layers	5457	6670	212	14.6	28	.96
5 Layers	9095	11046	212	14.7	28	1.48
Bandgap Structure	22280	29041	82	15.2	13	3.56
Reinforced Concrete						
Separated Bars	7984	9511	664	14.9	100	2.9
Connected Bars	6164	7340	664	14.6	100	2.62
Crossed Dipole FSS	4659	5696	352	14.8	50	1.16

Table II. Iterations and Execution Times for Test Cases

TEST CASE	Edges (N)	Edges in $\Gamma_z, \Gamma_{z+}$ (M)	Fill Time (min)	Iterations/N		Solve Time (min)	
				CGM	BCGM	CGM	BCGM
Inductive Screen	2244	290	1.62	.355	.057	1.87	.30
Wire Grid Array	7030	816	16.5	1.72	.084	147.5	7.38
Artificial Dielectric							
3 Layers	6670	212	3.63	.508	.063	16.78	2.53
5 Layers	11046	212	7.30	.699	.055	49.3	4.07
Bandgap Structure	29041	82	6.55	.792	.072	349	31.9
Reinforced Concrete							
Separated Bars	9511	664	.094	.78	.094	87.2	10.6
Connected Bars	7340	664	.162	.90	.162	64.7	13.1
Crossed Dipole FSS	4659	352	19.8	4.22	---	415.1	---

ing 5-12 times faster than the conjugate gradient solver. Unfortunately, the BCGM did not converge at all for several frequencies of the bandgap structure test case. It also failed to converge for any frequency of the crossed dipole FSS test case.

Figure 23 shows the convergence vs. frequency for the bandgap structure. CGM's variation is fairly regular, suggesting a systematic dependence on some feature of the problem that has not yet been identified. BCGM's variation with frequency is more random. The circles along the top of the graph mark those frequencies where BCGM failed to converge.

These execution statistics show that the HFEM technique can solve many practical problems in a reasonable time on a typical engineering workstation. A final important note is that its efficiency is much poorer than moment methods. Its use is justified when the problem geometry includes features that MoM cannot model.

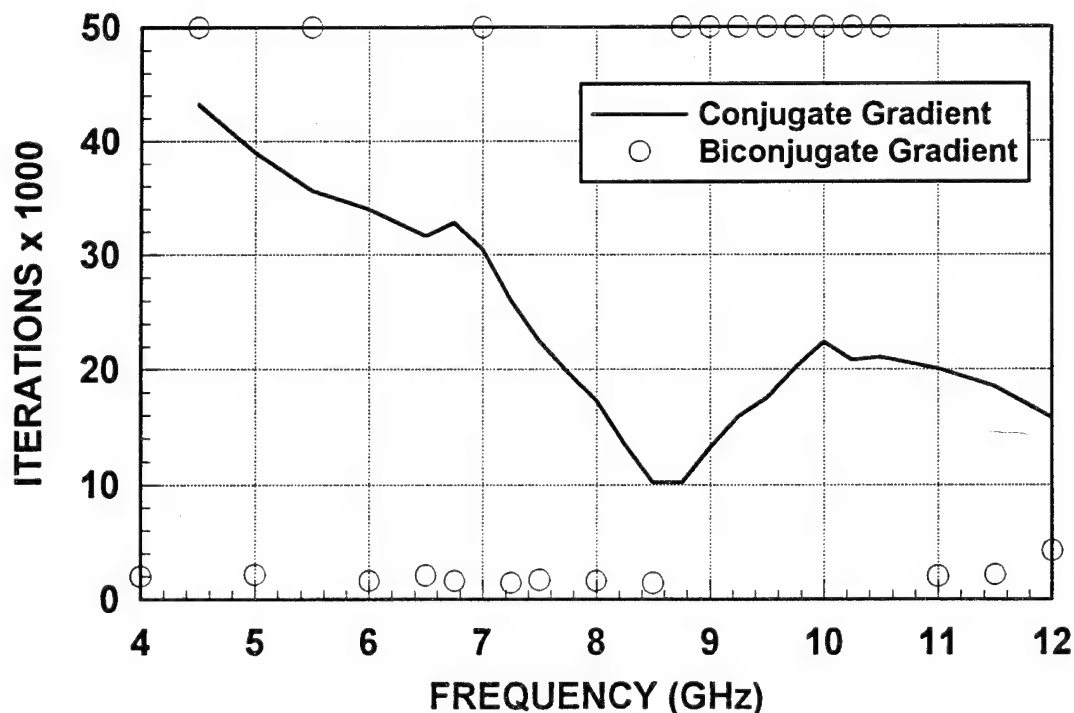


Figure 23. Number of Iterations vs. Frequency for Bandgap Structure Test Case



## 6. CONCLUSIONS AND RECOMMENDATIONS

The objective of this project in computational electromagnetics was to develop a method for predicting reflection and transmission from general periodic structures. The hybrid finite element method was selected because of its inherent ability to deal with inhomogeneous dielectrics and arbitrarily-oriented conductors. This report has discussed the theoretical basis in terms of the electric field wave equation with appropriate periodic boundary conditions, its translation into a numerical problem and matrix solution, its implementation in a general-purpose computer program, and finally, its results for a wide variety of validation cases. Those results show that the method is effective and reliable, although its efficiency relative to other methods is problem-dependent. The variety of validation cases accomplished with a single computer code demonstrates that HFEM is the most versatile tool to date for periodic structure analysis.

Recommendations for further work fall into two categories: exploiting the new code for problems of immediate interest to high power microwave research; and improvements to extend the code's range of usefulness and validity. Besides its demonstrated utility for reinforced concrete walls, the code may also be used to predict the shielding effectiveness of brick walls, including air pockets, perforated metal grids such as those used for equipment enclosures, and radomes and canopies that incorporate metallic grids for interference suppression. Artificial dielectrics may also be interesting for HPM antenna design, possibly replacing heavier natural dielectric lenses. But since the artificial dielectrics cause the fields passing through to become concentrated in between conducting elements, they may experience dielectric breakdown at much lower field levels. HFEM provides a unique tool for examining the electromagnetic field distribution in candidate structures and determining which are likely to be most useful.

RF shielding by composite materials made of graphite fibers embedded in a dielectric

material such as epoxy will become interesting in the future. For modeling those structures, it is more efficient to represent the graphite fibers as conducting filaments with a surface resistivity. Hence, a proposed extension to the computer code is to add conductors with finite conductivity. Second, it was observed that some problems experienced very slow convergence using the iterative matrix solvers. Those would benefit from implementation of a direct matrix solver using LU decomposition. However, that solver must take advantage of the matrix sparsity by starting with a row/column reordering such as the "minimum degree" algorithm [30] to minimize matrix fill in as the decomposition proceeds. Third, this periodic structure code is one of a family of three HFEM codes, the other two of which perform analyses of waveguide devices [31] and phased array antennas [6]. It is both possible and desirable to combine those capabilities in a single code. Finally, the crossed-dipole FSS test case illustrated a shortcoming of the present implementation of vector finite element solutions in regions that include field singularities. As an alternative to very fine meshing, which is computationally expensive, expansion functions ("singularity elements") that can model the singular behavior are preferred and should be developed.

## REFERENCES

1. Mittra, Raj, Chi H. Chan and Tom Cwik, "Techniques for Analyzing Frequency Selective Surfaces--A Review," *Proc. IEEE*, 12, pp. 1593-1615, Dec. 1988.
2. Pelton, Edward L. and Benadikt A. Munk, "A Streamlined Metallic Radome," *IEEE Trans. Antennas and Propagation*, AP-22, pp. 904-909, Sep. 1974.
3. Young, L., L.A. Robinson and C.A. Hacking, "Meander-line Polarizer," *IEEE Trans. Antennas and Propagation*, AP-21, pp. 376-378, Mar. 1973.
4. Cohn, Seymour, "Lens Type Radiators," *Antenna Engineering Handbook* (1st ed.), H. Jasik, editor, McGraw-Hill, 1961.
5. Franchi, Peter R. and Robert J. Mailloux, "Theoretical and Experimental Study of Metal Grid Angular Filters for Sidelobe Suppression," *IEEE Trans. Antennas and Propagation*, AP-31, pp. 445-450, May 1983.
6. McGrath, Daniel T., "Phased Array Antenna Analysis with Hybrid Finite Element Methods," PhD Dissertation, Air Force Institute of Technology, 1993.
7. Whitney, H., *Geometric Integration Theory*, Princeton NJ: Princeton Univ. Press, 1957.
8. Nedelec, J.C., "Mixed Finite Elements in  $R^3$ ," *Numerische Mathematik*, 35, pp. 315-341, 1980.
9. D'Angelo, John D. and Isaak D. Mayergoyz, "Finite Element Methods for the Solution of RF Radiation and Scattering Problems," *Electromagnetics*, 10, pp. 177-199, 1990.
10. Paulsen, K.D. and D.R. Lynch, "Elimination of Vector Parasites in Finite Element Maxwell Solutions," *IEEE Trans. Microwave Theory Tech.*, MTT-39, pp. 395-404, Mar. 1991.
11. Mur, Gerrit, "Finite Element Modeling of Three-Dimensional Electromagnetic Fields in Inhomogeneous Media," *Radio Science*, 26, pp. 275-280, 1991.
12. Silvester, P.P. and R.L. Ferrari, *Finite Elements for Electrical Engineers*, 2nd. ed., Cambridge Univ. Press, 1990.
13. Amitay, Noach, Victor Galindo and Chen-Pang Wu, *Theory and Analysis of Phased Array Antennas*, New York: Wiley, 1972.
14. Gedney, Steven D., Jin-Fa Lee and Raj Mittra, "A Combined FEM/MoM Approach to Analyze the Plane Wave Diffraction by Arbitrary Gratings," *IEEE Trans. Microwave Theory Tech.*, MTT-40, pp. 363-370, Feb. 1992.

15. Structural Dynamics Research Corp., *Integrated Design Engineering Analysis Software Users' Manual*, Milford OH: SDRC, 1990.
16. Sarkar, Tapan K. and Ercument Arvas, "On a Class of Finite Step Iterative Methods (Conjugate Directions) for the Solution of an Operator Equation Arising in Electromagnetics," *IEEE Trans. Antennas Propagat.*, **AP-33**, pp. 1058-1066, Oct. 1985.
17. Sarkar, Tapan K., "On the Application of the Generalized BiConjugate Gradient Method," *J. Electromagnetic Waves Appl.*, **1**, pp. 223-242, 1987.
18. Pissanetzky, S., *Sparse Matrix Technology*, New York: Academic Press, 1984.
19. Lee, Shung-Wu, Gino Zarillo and Chak-Lam Law, "Simple Formulas for Transmission Through Periodic Metal Grids or Plates," *IEEE Trans. Antennas and Propagation*, **AP-30**, pp. 904-910, Sept. 1982.
20. Lee, Shung-Wu, "Scattering by Dielectric Loaded Screen," *IEEE Trans. Antennas and Propagation*, **AP-19**, pp. 656-665, Sept. 1971.
21. Decker, Martin T., "Transmission and Reflection by a Parallel Wire Grid," *J. Res. Nat'l Bureau of Standards*, **63D**, pp. 87-90, Aug. 1959.
22. Wait, J.R., "Reflection at Arbitrary Incidence from a Parallel Wire Grid," *Appl. Sci. Research*, **4B**, p. 393, 1954.
23. Levin, L., "The Electrical Constants of a Material Loaded with Spherical Particles," *J. IEE*, pt. III, **94**, p. 65, 1947.
24. Yamamoto, Y. and S. Machida, "High-impedance suppression of pump fluctuations and amplitude squeezing in semiconductor lasers," *Phys. Rev. A*, **35**, p. 5114, 1987.
25. Yablonovitch, E., T.J. Gmitter, K.M. Leung, R.D. Meade, A.M. Rappe, K.D. Brommer and J.D. Joannopoulos, "3-Dimensional Photonic Band Structure," *Optical and Quantum Electronics*, **24**, pp. S273-S283, 1992.
26. Kelly, P.K., J.G. Maloney, B.L. Shirley and R.L. Moore, "Photonic Band Structures of Finite Thickness: Theory and Experiment," *1994 IEEE AP-S Symposium Digest*, Vol. 2, pp. 718-721, Jul. 1994.
27. Plihal, M. and A.A. Maradudin, "Photonic Band Structure of Two-dimensional Systems: The Triangular Lattice," *Phys. Rev. B*, **44**, pp. 8565-8571, Oct. 1991.

28. Munk, Benadikt A., Robert G. Kouyoumjian, and Leon Peters, Jr., "Reflection Properties of Periodic Surfaces of Loaded Dipoles," *IEEE Trans. Antennas Propagat.*, AP-19, pp. 612-617, Sept. 1971.
29. Cwik, Thomas A. and Raj Mittra, "Scattering from a Periodic Array of Free-Standing Arbitrarily Shaped Perfectly Conducting Patches," *IEEE Trans. Antennas Propagat.*, AP-35, pp. 1226-1234, Nov. 1967.
30. A. George and J.W.-H. Liu, "The Evolution of the Minimum Degree Ordering Algorithm," *SIAM Review*, 31, pp. 1-19, 1989.
31. McGrath, Daniel T., "Hybrid Finite Element/Waveguide Mode Analysis of Passive RF Devices," RL-TR-93-130, Griffiss AFB NY: Rome Laboratory, Jul. 1993.

# DISTRIBUTION LIST

AUL/LSE Maxwell AFB, AL	2 Cys	WL/XPN Wright-Patterson AFB, OH	2 Cys
DTIC/OCP Fort Belvoir, VA	2 Cys	WL/AARA Wright-Patterson AFB, OH	1 Cy
AFSAA/SAI Washington, DC	1 Cy	NASA Ames Research Ctr Moffett Field, CA	1 Cy
PL/SUL Kirtland AFB, NM	2 Cys	Caltech/JPL Pasadena, CA	1 Cy
PL/HO Kirtland AFB, NM	1 Cy	NRL Code 4050 Washington, DC	1 Cy
PL/CAW Kirtland AFB, NM	1 Cy	NAWC Code 3951 China Lake, CA	1 Cy
PL/WSA Kirtland AFB, NM	1 Cy	USAFA/DFEE USAFA, CO	1 Cy
PL/WSM Kirtland AFB, NM	3 Cys	Sandia Nat'l Lab Dept 9352 Albuquerque, NM	1 Cy
PL/WSR Kirtland AFB, NM	4 Cys	NCCOSC NRad 822 San Diego, CA	1 Cy
PL/WST Kirtland AFB, NM	2 Cys	Naval Postgraduate School Code EC/Jn Monterey, CA	1 Cy
RL/ERA Hanscom AFB, NM	2 Cys	AFIT/LDEE Wright-Patterson AFB, OH	1 Cy
RL/ERC Hanscom AFB, NM	1 Cy	RL/SUL Griffiss AFB, NY	1 Cy
RL/ERP Griffiss AFB, NY	1 Cy	DIA/MSIC Redstone Arsenal, AL	1 Cy
AFOSR/NM Bolling AFB, DC	1 Cy	AFIT/ENG Wright-Patterson AFB, OH	2 Cys
Official Record Copy PL/WSR	10 Cys		